

**This is a self-archived version of an original article. This version may differ from the original in pagination and typographic details.**

**Author(s):** Lv, B. F.; Petrache, C. M.; Zheng, K. K.; Zhang, Z. H.; Sun, W.; Li, Z. P.; He, X. T.; Zhang, J.; Astier, A.; Greenlees, P.; Grahn, T.; Julin, R.; Juutinen, S.; Luoma, M.; Ojala, J.; Pakarinen, J.; Partanen, J.; Rahkila, P.; Ruotsalainen, P.; Sandzelius, M.; Sarén, J.; Tann, H.; Uusitalo, J.; Zimba, G.; Cederwall, B.; Aktas, Ö.; Ertoprak, A.; Zhang, W.; Guo, S.; Liu, M. L.; Ong, H. J.; Sun, Z. Y.; Wang, J. G.; Zhou, X. H.; Kuti,

**Title:** Refined description of the positive-parity bands and the extent of octupole correlations in  $^{120}\text{Ba}$

**Year:** 2022

**Version:** Published version

**Copyright:** © 2022 American Physical Society (APS)

**Rights:** In Copyright

**Rights url:** <http://rightsstatements.org/page/InC/1.0/?language=en>

**Please cite the original version:**

Lv, B. F., Petrache, C. M., Zheng, K.K., Zhang, Z. H., Sun, W., Li, Z. P., He, X. T., Zhang, J., Astier, A., Greenlees, P., Grahn, T., Julin, R., Juutinen, S., Luoma, M., Ojala, J., Pakarinen, J., Partanen, J., Rahkila, P., Ruotsalainen, P., . . . Page, R. D. (2022). Refined description of the positive-parity bands and the extent of octupole correlations in  $^{120}\text{Ba}$ . *Physical Review C*, 105(4), Article 044319. <https://doi.org/10.1103/PhysRevC.105.044319>

# Refined description of the positive-parity bands and the extent of octupole correlations in $^{120}\text{Ba}$

B. F. Lv,<sup>1,2</sup> C. M. Petrache,<sup>2,\*</sup> K. K. Zheng,<sup>2,1</sup> Z. H. Zhang,<sup>3</sup> W. Sun,<sup>4</sup> Z. P. Li,<sup>4</sup> X. T. He,<sup>5</sup> J. Zhang,<sup>5</sup> A. Astier,<sup>2</sup> P. Greenlees,<sup>6</sup> T. Grahm,<sup>6</sup> R. Julin,<sup>6</sup> S. Juutinen,<sup>6</sup> M. Luoma,<sup>6</sup> J. Ojala,<sup>6</sup> J. Pakarinen,<sup>6</sup> J. Partanen,<sup>6</sup> P. Rähkila,<sup>6</sup> P. Ruotsalainen,<sup>6</sup> M. Sandzelius,<sup>6</sup> J. Sarén,<sup>6</sup> H. Tann,<sup>6,7</sup> J. Uusitalo,<sup>6</sup> G. Zimba,<sup>6</sup> B. Cederwall,<sup>8</sup> Ö. Aktas,<sup>8</sup> A. Ertoprak,<sup>8</sup> W. Zhang,<sup>8</sup> S. Guo,<sup>1,9</sup> M. L. Liu,<sup>1,9</sup> H. J. Ong,<sup>1,9</sup> Z. Y. Sun,<sup>1,9</sup> J. G. Wang,<sup>1,9</sup> X. H. Zhou,<sup>1,9</sup> I. Kuti,<sup>10</sup> B. M. Nyakó,<sup>10</sup> D. Sohler,<sup>10</sup> J. Timár,<sup>10</sup> C. Andreoiu,<sup>11</sup> M. Doncel,<sup>7</sup> D. T. Joss,<sup>7</sup> and R. D. Page<sup>7</sup>

<sup>1</sup>Key Laboratory of High Precision Nuclear Spectroscopy and Center for Nuclear Matter Science, Institute of Modern Physics, Chinese Academy of Sciences, Lanzhou 730000, China

<sup>2</sup>Université Paris-Saclay, CNRS/IN2P3, IJCLab, 91405 Orsay, France

<sup>3</sup>Mathematics and Physics Department, North China Electric Power University, Beijing 102206, China

<sup>4</sup>School of Physical Science and Technology, Southwest University, Chongqing 400715, China

<sup>5</sup>College of Materials Science and Technology, Nanjing University of Aeronautics and Astronautics, Nanjing 210016, China

<sup>6</sup>Department of Physics, University of Jyväskylä, Jyväskylä FIN-40014, Finland

<sup>7</sup>Oliver Lodge Laboratory, Department of Physics, University of Liverpool, Liverpool L69 7ZE, United Kingdom

<sup>8</sup>KTH Department of Physics, S-10691 Stockholm, Sweden

<sup>9</sup>School of Nuclear Science and Technology, University of Chinese Academy of Science, Beijing 100049, China

<sup>10</sup>Institute for Nuclear Research (Atomki), Pf. 51, 4001 Debrecen, Hungary

<sup>11</sup>Department of Chemistry, Simon Fraser University, Burnaby, BC V5A 1S6, Canada



(Received 26 November 2021; revised 20 March 2022; accepted 28 March 2022; published 20 April 2022)

Three new negative-parity bands have been identified in  $^{120}\text{Ba}$ , two of them forming a strongly coupled band. The previously known negative-parity band is significantly extended to high spin, while the lower part of the yrare positive-parity band has been modified. From the analysis of the band properties and comparison with the neighboring nuclei a coherent description of all bands is achieved. In particular, a simple explanation of the evolution of the positive-parity bands at high spin is proposed, including the possible occupation of the  $\nu f_{7/2}[541]1/2^-$  intruder orbital. Cranked Nilsson-Strutinsky calculations reveal similar quadrupole deformations but different triaxiality of the bands, while particle number conserving cranked shell model calculations qualitatively reproduce the experimental data and support the assigned configurations. The new measured ratios of reduced transition probabilities  $B(E1)/B(E2)$  complete the systematics in the  $^{118-124}\text{Ba}$  nuclei, exhibiting a decrease with decreasing neutron number, and are compared with the known values in the  $^{116-120}\text{Xe}$  nuclei, which are larger. Extended calculations with the quadrupole and octupole collective Hamiltonian based on the relativistic Hartree-Bogoliubov model employing the relativistic DD-PC1 density functional nicely reproduce the decreasing trend towards lower neutron numbers for Ba and Xe nuclei, as well as the larger values in Xe nuclei, but are much larger in amplitude than the experimental values. On the other hand, particle number conserving cranked shell model calculations without octupole deformation overestimate the low-spin values, while those with octupole deformation included reproduce the experimental values in  $^{120}\text{Ba}$ , suggesting the possible existence of moderate octupole collectivity in the negative-parity bands of nuclei in this mass region.

DOI: [10.1103/PhysRevC.105.044319](https://doi.org/10.1103/PhysRevC.105.044319)

## I. INTRODUCTION

To date, only a few rotational bands are known in the lightest even-even barium isotopes  $^{118,120}\text{Ba}$  [1,2]. Two peculiar features have been reported in these nuclei: possible existence of enhanced octupole correlations in  $^{118}\text{Ba}$  [1] and  $^{124}\text{Ba}$  [3] due to the close proximity of the Fermi level to orbitals from both the  $\pi h_{11/2}$  and  $\pi d_{5/2}$  subshells, which are characterized by differences in angular momentum  $\Delta l = \Delta j = 3$ , and an unique phenomenon at high spin in  $^{120}\text{Ba}$  exhibiting forking

of the ground-state band into two two-quasiparticle bands built on  $\pi(h_{11/2})^2$  and  $\nu(h_{11/2})^2$  configurations, and their successive recombination of the aligned bands into a four-quasiparticle  $\pi(h_{11/2})^2 \otimes \nu(h_{11/2})^2$  band [2]. Total Routhian surface (TRS) and cranked shell model calculations could not give a comprehensive understanding of the structure and alignment properties of the two- and four-quasiparticle bands observed in  $^{120}\text{Ba}$  [2], while the evidence of octupole correlations in the negative-parity band observed in  $^{118}\text{Ba}$  was tentative [1], due to limited experimental information. The remaining open questions in these proton-rich nuclei were also due to the poor knowledge of the favored one-quasiparticle configurations, since only two bands were known in each

\*Corresponding author: petrache@ijclab.in2p3.fr

of the odd-even  $^{117,119}\text{Ba}$  and  $^{117,119}\text{Cs}$  neighboring nuclei. However, the band structures of  $^{119}\text{Ba}$  and  $^{119}\text{Cs}$  have been significantly enriched recently: several rotational bands and isomeric states have been identified in both nuclei [4,5], with excitation energies, spins and parities established experimentally. These new results offer an unique opportunity, rarely available close to the proton drip line, to compare the observed bands in the even-even  $^{120}\text{Ba}$  nucleus with those obtained from the juxtaposition of configurations observed in the odd-even neighboring nuclei. Such a comparison can constrain the number of suitable configurations and give confidence in the assigned ones. The  $^{120}\text{Ba}$  nucleus is particularly interesting among the nuclei close to the proton drip line because of the exotic phenomenon of forking and recombination of the ground-state band [2]. In addition, based on the successful description of the rotational bands in the neighboring  $^{119}\text{Ba}$  and  $^{119}\text{Cs}$  nuclei [4,5] under the assumption of a large quadrupole deformation of  $\varepsilon_2 = 0.32$ , based on the measured spectroscopic quadrupole moments [6,7], the occupation of neutron down-sloping intruder orbitals significantly impact the high-spin band properties and therefore have to be taken into account. This motivated us to undertake a study of the band structure of  $^{120}\text{Ba}$ , with the aim to gather additional experimental information and try to better understand the band structures, including the negative-parity ones, which are expected to exhibit enhanced octupole correlations.

We report results on three new bands in  $^{120}\text{Ba}$ , two being nearly degenerate and forming a strongly coupled band. The previously known negative-parity band [8] is considerably extended to high spin. The configurations of the observed bands are assigned based on the analysis of the alignment properties of the bands, on the comparison with the odd-even neighboring  $^{119}\text{Ba}$  and  $^{119}\text{Cs}$  nuclei, on systematics, as well as on cranked Nilsson-Strutinsky (CNS) [9–12], particle number conserving cranked shell model (PNC-CSM) without octupole deformation [13,14] and with octupole deformation included [15], as well as quadrupole and octupole collective Hamiltonian based on the relativistic Hartree-Bogoliubov (QOCH-RHB) [16] calculations using the DD-PC1 density functional [17].

## II. EXPERIMENTAL DETAILS AND RESULTS

The presently reported results have been obtained in an experiment performed with the high-efficiency  $\gamma$ -ray detector array JUROGAM 3 [18] and the recoil mass separator MARA [19], using the  $^{58}\text{Ni}(^{64}\text{Zn}, 2p)^{120}\text{Ba}$  fusion-evaporation reaction. A 255-MeV beam of  $^{64}\text{Zn}$  was provided by the K130 cyclotron at the Accelerator Laboratory of the University of Jyväskylä, Finland. A self-supporting enriched  $^{58}\text{Ni}$  foil of 0.75 mg/cm<sup>2</sup> thickness was used as a target. The data were collected by the triggerless total data readout (TDR) data acquisition system [20] and sorted using the GRAIN code [21]. The data were analyzed using the RADWARE [22,23] package. More experimental details are given in Ref. [5]. It is worth to mention that the definition of the directional correlation from

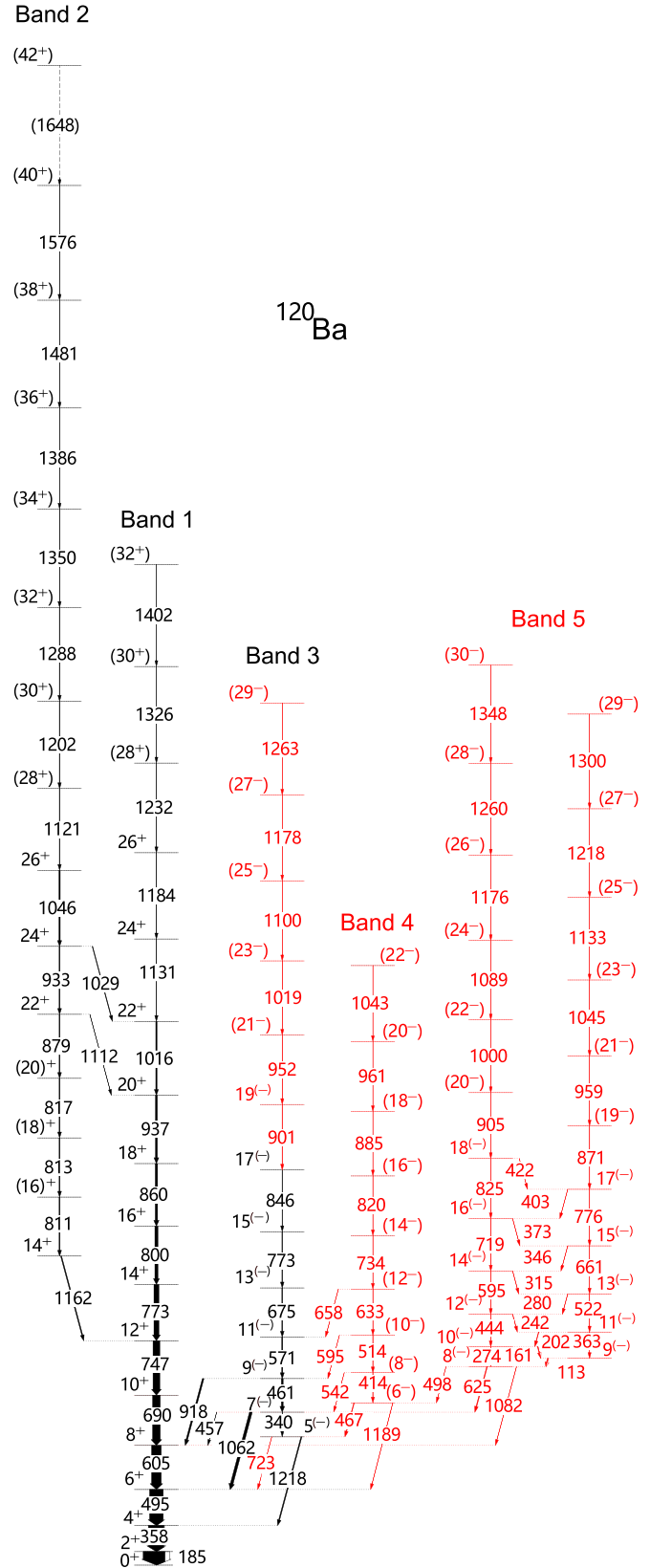


FIG. 1. Level scheme of  $^{120}\text{Ba}$  resulting from the present work. The new transitions are indicated in red. The tentative spins and parities are given in parentheses.

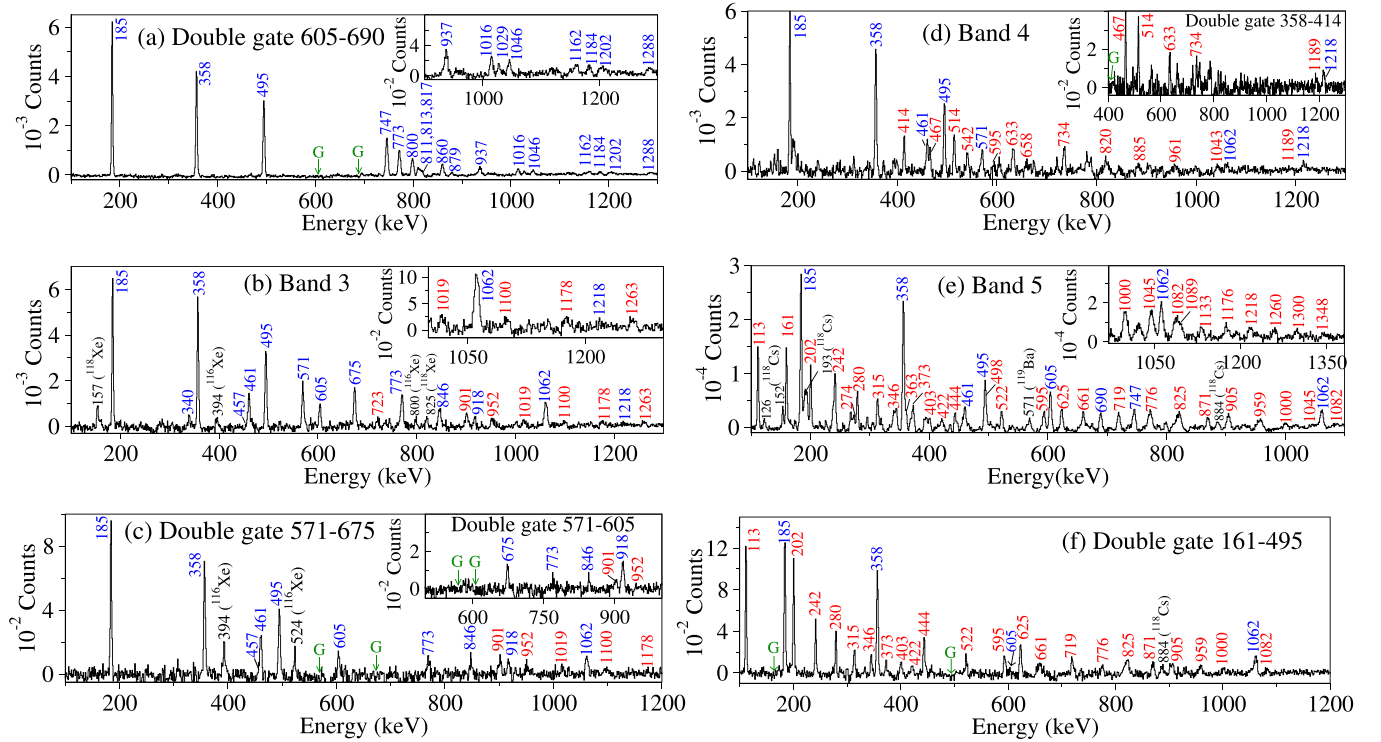


FIG. 2. Double-gated spectra from  $\gamma\gamma\gamma$  coincidences measured with only JUROGAM 3, without conditions on the mass spectra detected at the MARA focal plane. Peak energies are in blue, red, and black for previously known, new and contaminant transitions, respectively, while the gating transitions are indicated in green with “G” when only one double gate was used. (a) Spectrum double gated on the 605- and 690-keV transitions of Band 1, showing in-band transitions up to 1288 keV, with a zoom in the high-energy part in the inset. (b) Spectrum for Band 3 obtained by summing the spectra double gated on any combination of the 185-, 358-, 495-keV transitions of Band 1, and of the 340-, 461-, 571-, 846-, 901-, 952-, 1019-, 1062-, 1100-, 1178-, 1263-keV transitions of Band 3, with a zoom in the high-energy part in the inset. (c) Spectrum double gated on the 571- and 675-keV transitions, and, in the inset, the spectrum double gated on the 571- and 605-keV transitions of Bands 3 and 1, respectively. (d) Spectrum for Band 4 obtained by summing the spectra double gated on the 185-, 358-, 495-keV transitions of Band 1 and on the 467-, 414-, 514-, 633-, 734-, 820-, 1218-keV in-band and the connecting transitions to Bands 1 and 3, and, in the inset, the spectrum double gated on the 358- and 414-keV transitions of Bands 1 and 4, respectively. (e) Spectrum for Band 5 obtained by summing the double gated spectra on all in-band  $E2$  and the interconnecting transitions of the two cascades of Band 5, and on the 185-, 358-, 495-, and 605-keV transitions of Band 1, and, in the inset, the high-energy part of the spectrum for Band 5 obtained by summing the spectra double gated on all in-band  $E2$  and the interconnecting transitions of the two  $E2$  cascades. (f) Spectrum double gated on the 161- and 495-keV transitions of Bands 5 and 1, respectively.

oriented states (DCO) ratios ( $R_{DCO}$ ) and two-point angular correlation (anisotropy) ratios  $R_{ac}$  are exactly the same as in Ref. [5].

The level scheme of  $^{120}\text{Ba}$  is shown in Fig. 1. Energy spectra obtained from prompt  $\gamma\gamma\gamma$  coincidences showing the transitions of the newly identified bands, as well as the complete experimental information on the  $\gamma$ -ray transitions are given in Fig. 2 and in the Table I.

The level scheme was constructed based on the detailed analysis of the coincidence relationships between the  $\gamma$  rays and their intensities measured with JUROGAM 3. The previously reported connecting transitions of Band 3 are confirmed [2], and a weak transition of 723 keV was newly identified, as shown in Fig. 2(b). The spectrum double gated on the 571- and 675-keV transitions in Fig. 2(c) shows the 457-, 918-, and 1062-keV connecting transitions to Band 1. The spectrum double gated on the 571- and 605-keV transitions of Bands 3 and 1, respectively, shown in the inset of Fig. 2(c),

clearly shows the 918-keV transition and fixes its position in the level scheme. The connecting transitions of Band 4 of 467, 542, 595, 658, and 1189 keV can be seen in Fig. 2(d), while those of Band 5 of 498, 625 and 1089 keV can be seen in Fig. 2(e). In Fig. 2(f) a spectrum gated on the 161- and 495-keV transitions clearly show the 1082-keV transition, which is composed of a doublet in the spectrum of Fig. 2(e).

The previously known positive-parity Bands 1 and 2 are confirmed up to the highest observed states, with transition energies, which in some cases differ from those reported in Ref. [2] by up to 3 keV. By analyzing the relative intensities of the 811-, 813-, and 817-keV transitions in Band 2, we tentatively changed their order relative to that of Ref. [2], which leads to a gradual increase of the transition energies with increasing spin and therefore to a smooth variation of the band properties in the crossing region, as expected for well-deformed nuclei in which the two configurations before and after the crossing are strongly mixed (see Figs. 3 and 4).

TABLE I. Experimental information including the  $\gamma$ -ray energies  $E_\gamma$ , energies of the initial levels  $E_i$ , relative intensities  $I_\gamma$ ,  $R_{DCO}$  ratios and/or anisotropies  $R_{ac}$ , and the spin-parity assignments to the observed states in  $^{120}\text{Ba}$ .

$E_\gamma$ (keV)	$E_i$ (keV)	$I_\gamma^b$	$R_{DCO}^c$	$R_{ac}^d$	Multipolarity	$J_i^\pi \rightarrow J_f^\pi$
<b>Band 1</b>						
185.2(1)	185.2(1)	100.0	1.04(7) <sup>d</sup>		$E2$	$2^+ \rightarrow 0^+$
357.8(2)	543.0(2)	72(4)	1.0(1) <sup>d</sup>		$E2$	$4^+ \rightarrow 2^+$
495.2(2)	1038.2(3)	62(4)	1.0(1) <sup>d</sup>		$E2$	$6^+ \rightarrow 4^+$
605.3(3)	1643.5(4)	44(2)	1.0(1) <sup>d</sup>		$E2$	$8^+ \rightarrow 6^+$
690.2(2)	2333.7(5)	35(3)	1.0(1) <sup>d</sup>		$E2$	$10^+ \rightarrow 8^+$
747.2(2)	3080.9(5)	31(4)	1.0(1) <sup>d</sup>		$E2$	$12^+ \rightarrow 10^+$
773.1(4)	3854.0(6)	23(2)	1.0(1) <sup>d</sup>		$E2$	$14^+ \rightarrow 12^+$
800.4(5)	4654.4(8)	14(2)	0.9(2) <sup>d</sup>		$E2$	$16^+ \rightarrow 14^+$
860.0(6)	5514.4(10)	11(1)	1.1(1) <sup>d</sup>		$E2$	$18^+ \rightarrow 16^+$
937.4(8)	6451.8(13)	8.8(7)	1.0(1) <sup>d</sup>		$E2$	$20^+ \rightarrow 18^+$
1015.6(9)	7467.4(16)	5.7(9)	1.0(1) <sup>d</sup>		$E2$	$22^+ \rightarrow 20^+$
1131.3(10)	8598.7(19)	1.9(4)	1.0(2) <sup>d</sup>		$E2$	$24^+ \rightarrow 22^+$
1183.9(14)	9782.6(23)	1.6(3)	1.2(3) <sup>d</sup>		$E2$	$26^+ \rightarrow 24^+$
1231.8(13)	11014.4(27)	1.2(3)				$(28^+) \rightarrow (26^+)$
1326.0(17)	12340.4(32)	0.5(2)				$(30^+) \rightarrow (28^+)$
1402.2(18)	13742.6(36)	<0.1				$(32^+) \rightarrow (30^+)$
<b>Band 2</b>						
810.8(5)	5054.0(11)	4.3(6)				$16^+ \rightarrow 14^+$
813.3(8)	5867.3(13)	4.1(7)				$18^+ \rightarrow 16^+$
817.1(6)	6684.4(15)	4.0(5)				$20^+ \rightarrow 18^+$
879.2(5)	7563.6(15)	3.9(4)		1.3(1)	$E2$	$22^+ \rightarrow 20^+$
933.1(7)	8496.7(17)	4.2(3)		1.4(2)	$E2$	$24^+ \rightarrow 22^+$
1029.1(7)	8496.7(17)	2.5(3)		1.3(3)	$E2$	$24^+ \rightarrow 22^+$
1045.5(8)	9542.2(19)	5.8(4)		1.4(3)	$E2$	$26^+ \rightarrow 24^+$
1112.1(7)	7563.6(15)	0.6(2)		1.6(5)	$E2$	$22^+ \rightarrow 20^+$
1121.2(9)	10663.4(21)	2.5(4)				$(28^+) \rightarrow 26^+$
1162.3(8)	4243.2(9)	4.5(3)		1.3(1)	$E2$	$14^+ \rightarrow 12^+$
1201.6(9)	11865.0(23)	2.4(2)				$(30^+) \rightarrow (28^+)$
1288.1(13)	13153.1(26)	2.3(3)				$(32^+) \rightarrow (30^+)$
1349.7(17)	14502.8 (31)	1.6(3)				$(34^+) \rightarrow (32^+)$
1386.4(19)	15889.2(37)	0.7(2)				$(36^+) \rightarrow (34^+)$
1481.2(22)	17370.4(43)	0.3(2)				$(38^+) \rightarrow (36^+)$
1575.9(21)	18946.3(48)	<0.1				$(40^+) \rightarrow (38^+)$
1648.0(24)	20594.3(53)	<0.1				$(42^+) \rightarrow (40^+)$
<b>Band 3</b>						
339.7(2)	2100.4(11)	1.1(2)	0.9(2) <sup>d</sup>		$E2$	$7^{(-)} \rightarrow 5^{(-)}$
457.1(3)	2100.4(11)	<0.1				$7^{(-)} \rightarrow 8^+$
461.0(2)	2561.4(11)	8.1(9)	1.1(1) <sup>d</sup>		$E2$	$9^{(-)} \rightarrow 7^{(-)}$
570.6(4)	3132.0(12)	4.8(5)	0.9(1) <sup>d</sup>		$E2$	$11^{(-)} \rightarrow 9^{(-)}$
674.9(5)	3806.9(13)	3.6(3)	1.1(2) <sup>d</sup>		$E2$	$13^{(-)} \rightarrow 11^{(-)}$
722.8(7)	1760.7(9)	0.6(3)				$5^{(-)} \rightarrow 6^+$
772.6(5)	4579.5(15)	2.9(6)	0.9(2) <sup>d</sup>		$E2$	$15^{(-)} \rightarrow 13^{(-)}$
846.2(6)	5425.7(16)	1.5(2)	1.2(2) <sup>d</sup>		$E2$	$17^{(-)} \rightarrow 15^{(-)}$
900.7(7)	6326.4(17)	1.4(3)	1.1(2) <sup>d</sup>		$E2$	$19^{(-)} \rightarrow 17^{(-)}$
918.2(9)	2561.4(11)	7.0(7)		0.8(1)	(E1)	$9^{(-)} \rightarrow 8^+$
951.8(8)	7278.2(19)	0.8(3)				$(21^-) \rightarrow 19^{(-)}$
1019.4(9)	8297.6(21)	0.6(3)				$(23^-) \rightarrow (21^-)$
1062.2(6)	2100.4(11)	12(1)		0.7(1)	(E1)	$7^{(-)} \rightarrow 6^+$
1099.6(11)	9397.2(24)	0.3(1)				$(25^-) \rightarrow (23^-)$
1178.2(9)	10575.4(25)	0.14(6)				$(27^-) \rightarrow (25^-)$
1217.7(9)	1760.7(9)	2.2(5)		0.6(2)	(E1)	$5^{(-)} \rightarrow 4^+$
1263.2(13)	11838.6(29)	<0.1				$(29^-) \rightarrow (27^-)$
<b>Band 4</b>						
414.4(2)	2641.8(10)	1.1(3)		1.5(2)	$E2$	$(8^-) \rightarrow (6^-)$
466.7(4)	2227.4(10)	1.5(4)		1.1(3)	$M1/E2$	$(6^-) \rightarrow 5^{(-)}$

TABLE I. (*Continued.*)

$E_\gamma$ (keV)	$E_i$ (keV)	$I_\gamma^b$	$R_{DCO}^c$	$R_{ac}^d$	Multipolarity	$J_i^\pi \rightarrow J_f^\pi$
514.3(4)	3156.1(11)	1.3(2)		1.3(2)	$E2$	$(10^-) \rightarrow (8^-)$
541.8(5)	2641.8(10)	0.3(1)				$(8^-) \rightarrow 7^{(-)}$
595.1(6)	3156.1(11)	0.4(2)				$(10^-) \rightarrow 9^{(-)}$
633.4(7)	3789.5(13)	0.9(2)				$(12^-) \rightarrow (10^-)$
657.9(8)	3789.5(13)	0.2(1)				$(12^-) \rightarrow 11^{(-)}$
$E_\gamma$ (keV)	$E_i$ (keV)	$I_\gamma^a$	$R_{DCO}^b$	$R_{ac}^c$	Multipolarity	$J_i^\pi \rightarrow J_f^\pi$
734.4(6)	4523.9(14)	0.6(1)				$(14^-) \rightarrow (12^-)$
820.4(6)	5344.3(16)	0.5(2)				$(16^-) \rightarrow (14^-)$
884.8(5)	6229.1(16)	0.3(1)				$(18^-) \rightarrow (16^-)$
960.8(7)	7189.9(18)	<0.1				$(20^-) \rightarrow (18^-)$
1043.2(9)	8233.1(20)	<0.1				$(22^-) \rightarrow (20^-)$
1189.1(9)	2227.4(10)	0.4(2)				$(6^-) \rightarrow 6^+$
Band 5						
113.0(1)	2838.6(11)	3.5(4)	0.8(2) <sup>e</sup>		$M1/E2$	$9^{(-)} \rightarrow 8^{(-)}$
161.0(2)	2999.6(12)	2.5(4)	0.9(1) <sup>e</sup>		$M1/E2$	$10^{(-)} \rightarrow 9^{(-)}$
201.8(1)	3201.4(12)	1.9(2)	0.9(1) <sup>e</sup>		$M1/E2$	$11^{(-)} \rightarrow 10^{(-)}$
242.3(2)	3443.7(12)	1.3(3)	1.0(1) <sup>e</sup>		$M1/E2$	$12^{(-)} \rightarrow 11^{(-)}$
274.3(3)	2999.6(12)	0.5(1)				$10^{(-)} \rightarrow 8^{(-)}$
280.1(1)	3723.8(12)	1.0(2)	1.2(2) <sup>e</sup>		$M1/E2$	$13^{(-)} \rightarrow 12^{(-)}$
315.1(4)	4038.9(13)	0.9(1)	1.2(2) <sup>e</sup>		$M1/E2$	$14^{(-)} \rightarrow 13^{(-)}$
345.7(2)	4384.6(13)	0.6(1)	1.1(3) <sup>e</sup>		$M1/E2$	$15^{(-)} \rightarrow 14^{(-)}$
362.9(4)	3201.4(12)	0.9(2)		1.3(2)	$E2$	$11^{(-)} \rightarrow 9^{(-)}$
373.1(5)	4757.7(14)	0.6(2)				$16^{(-)} \rightarrow 15^{(-)}$
403.2(5)	5160.6(15)	0.5(1)				$17^{(-)} \rightarrow 16^{(-)}$
422.3(3)	5583.0(15)	0.3(1)				$18^{(-)} \rightarrow 17^{(-)}$
444.2(4)	3443.7(12)	1.0(2)		1.5(2)	$E2$	$12^{(-)} \rightarrow 10^{(-)}$
497.8(12)	2725.6(11)	0.3(2)				$8^{(-)} \rightarrow (6^-)$
522.2(3)	3723.8(12)	1.0(2)		1.4(3)	$E2$	$13^{(-)} \rightarrow 11^{(-)}$
595.0(4)	4038.9(13)	1.0(2)		1.4(2)	$E2$	$14^{(-)} \rightarrow 12^{(-)}$
625.2(3)	2725.6(11)	3.3(4)		0.7(1)	$M1/E2$	$8^{(-)} \rightarrow 7^{(-)}$
661.1(5)	4384.6(13)	1.0(2)		1.4(3)	$E2$	$15^{(-)} \rightarrow 13^{(-)}$
719.1(5)	4757.7(14)	1.2(2)		1.3(1)	$E2$	$16^{(-)} \rightarrow 14^{(-)}$
776.0(7)	5160.6(15)	0.9(2)		1.5(2)	$E2$	$17^{(-)} \rightarrow 15^{(-)}$
825.3(6)	5583.0(15)	0.6(1)		1.3(2)	$E2$	$18^{(-)} \rightarrow 16^{(-)}$
870.6(8)	6031.2(17)	0.7(2)				$(19^-) \rightarrow 17^{(-)}$
904.8(9)	6487.8(18)	0.3(1)				$(20^-) \rightarrow 18^{(-)}$
958.9(9)	6990.1(19)	0.6(2)				$(21^-) \rightarrow (19^-)$
999.8(8)	7487.6(20)	0.2(1)				$(22^-) \rightarrow (20^-)$
1045.2(9)	8035.3(21)	0.4(2)				$(23^-) \rightarrow (21^-)$
1082.3(14)	2725.6(11)	0.4(2)				$8^{(-)} \rightarrow 8^+$
1088.6(13)	8576.2(23)	0.19(6)				$(24^-) \rightarrow (22^-)$
1133.4(11)	9168.7(24)	0.2(1)				$(25^-) \rightarrow (23^-)$
1175.6(15)	9751.8(28)	0.15(5)				$(26^-) \rightarrow (24^-)$
1217.5(16)	10386.2(29)	0.17(4)				$(27^-) \rightarrow (25^-)$
1259.8(16)	11011.6(32)	0.10(5)				$(28^-) \rightarrow (26^-)$
1300.4(19)	11686.6(34)	0.11(7)				$(29^-) \rightarrow (27^-)$
1348.2(21)	12359.8(38)	<0.1				$(30^-) \rightarrow (28^-)$

<sup>a</sup>Relative intensities corrected for efficiency, normalized to the intensity of the 185.2-keV transition. The transition intensities were obtained from a combination of total projection and gated spectra.

<sup>b</sup> $R_{DCO}$  has been deduced from an asymmetric  $\gamma - \gamma$  coincidence matrix sorted with the detectors at  $157.6^\circ$  on one axis, and detectors at  $\approx 90^\circ$  on the other axis. The tentative spin-parity of the states are given in parentheses.

<sup>c</sup> $R_{ac}$  has been deduced from two asymmetric  $\gamma - \gamma$  coincidence matrices sorted with the detectors at  $133.6^\circ$  and  $157.6^\circ$  on one axis, and detectors at  $\approx 90^\circ$  on the other axis. The tentative spin-parity of the states are given in parentheses.

<sup>d</sup>DCO ratios for Band 1 deduced from the spectrum gated on the stretched quadrupole 185-, 358-, 605-, 860-, and 1131-keV transitions. DCO ratios for Band 3 deduced from the spectrum gated on the stretched quadrupole 461- and 846-keV transitions.

<sup>e</sup>DCO ratios for Band 5 deduced from the spectrum gated on the dipole 131-, 161-, 280-, and 315-keV transitions.



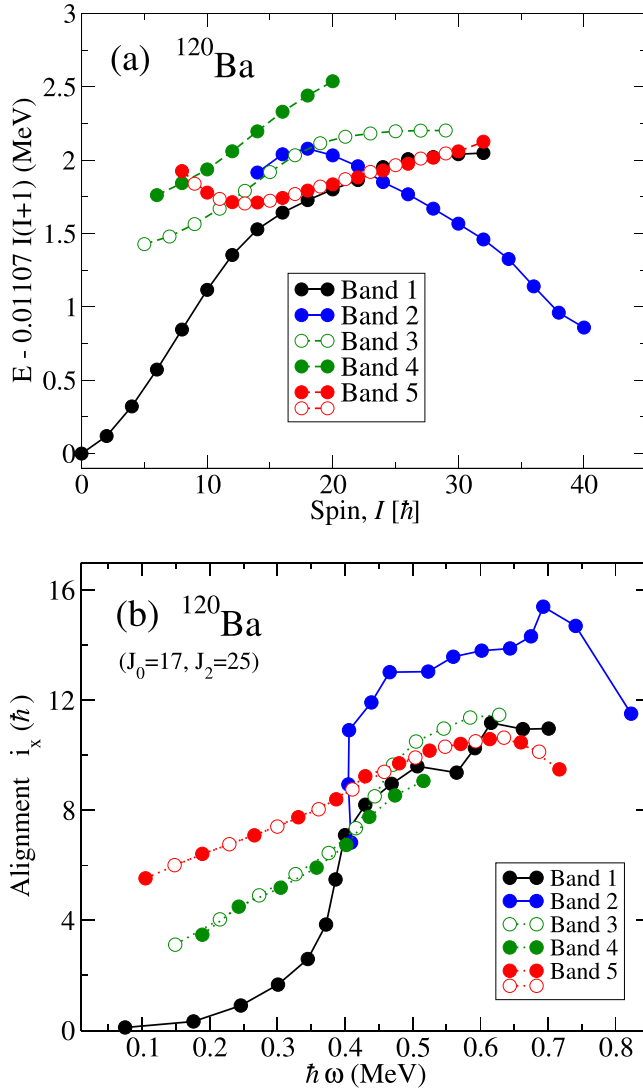


FIG. 3. (a) Excitation energies relative to a rigid rotor for the bands of  $^{120}\text{Ba}$ . (b) Single-particle aligned angular momenta  $i_x$  as function of the rotational frequency  $\hbar\omega$  for the observed bands in  $^{120}\text{Ba}$ . The angular momentum of the core is parametrized with the Harris parameters  $\mathcal{J}_0 = 17 \hbar^2 \text{MeV}^{-1}$  and  $\mathcal{J}_2 = 25 \hbar^4 \text{MeV}^{-3}$ . The  $K$  values are chosen in agreement with their assigned configurations: 0 for Bands 1 and 2, 3 for Bands 3 and 4, and 6 for Band 5. Filled (open) symbols indicate states with even (odd) spins, continuous (dashed) lines indicate positive (negative) parities.

Bands 3 and 4 are composed of cascades of  $E2$  transitions up to spin parities of  $(29^-)$  and  $(22^-)$ , respectively. The angular correlation results indicate dipole character for the 918-, 1062-, and 1218-keV transitions from Band 3 to Band 1, thus fixing odd spins for Band 3. Based on the systematics of the energy levels in the neighboring nuclei (see Fig. 5), and on the calculations given in the following discussion section, we assume that the connecting transitions have  $E1$  character, and therefore assign negative parity to Band 3. The angular correlation results for the connecting transitions of Band 4 to Bands 1 and 3 are not conclusive due to insufficient statistics and

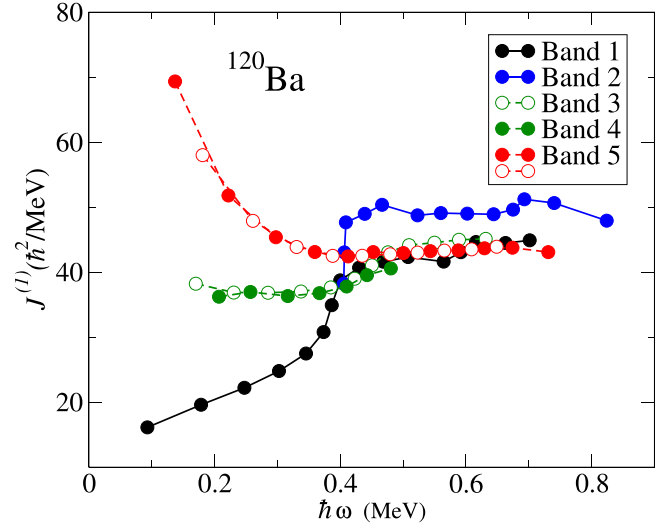


FIG. 4. Experimental moments of inertia  $J^{(1)}$  for all bands of  $^{120}\text{Ba}$ . The states with signature  $\alpha = 0$  and  $\alpha = 1$  are drawn with filled and open symbols, respectively.

contaminations. However, an  $E2$  character for the connecting transitions to Band 3 would lead to nearly degenerate levels of Bands 3 and 4, which would induce similar population intensity. This is in disagreement with the measured relative intensity of Band 4, which is an order of magnitude lower than that of Band 3. Therefore we tentatively assign  $M1/E2$  character to the connecting transitions between Bands 3 and 4, which leads to even spins and negative parity for Band 4.

Band 5 consists of two cascades of quadrupole transitions, which are interconnected by dipole transitions up to spin 18. It decays to the  $7^{(-)}$  state of Band 3, to the  $(6^-)$  state of Band 4, and to the  $8^+$  state of Band 1 via the 625-, 498-, and 1082-keV transitions, respectively. The 625-keV transition has a dipole character, which fixes spin 8 for the band head of Band 5, to which we tentatively assign negative parity, based on the comparison with the lowest observed configurations in  $^{119}\text{Cs}$  [5,24,25], on the systematics of such bands observed in neighboring  $^{122,124}\text{Ba}$  [3,26,27] and  $^{116,118,120}\text{Xe}$  [28,29] nuclei, on the band properties (excitation energies relative to a rigid rotor  $E - 0.01107I(I+1)$ , single-particle aligned angular momenta  $i_x$  and moments of inertia  $J^{(1)}$ ), and on the PNC-CSM calculations given in the following discussion section.

### III. DISCUSSION

#### A. General analysis

The plot of excitation energies relative to a rigid rotor  $E - 0.01107I(I+1)$  [11] shown in Fig. 3(a) give a first global view of the band structures. One can see that Band 1 after the up-bend observed at spin  $I^\pi \approx 10^+$  ( $\hbar\omega \approx 0.4 \text{ MeV}$ ) is nearly degenerate with the strongly coupled Band 5, that the low-spin part of Band 2 is nearly degenerate with Band 3, that Band 4 is excited by  $\approx 0.3 \text{ MeV}$  relative to Band 3, and the high-spin part of Band 2, which has a slope opposite

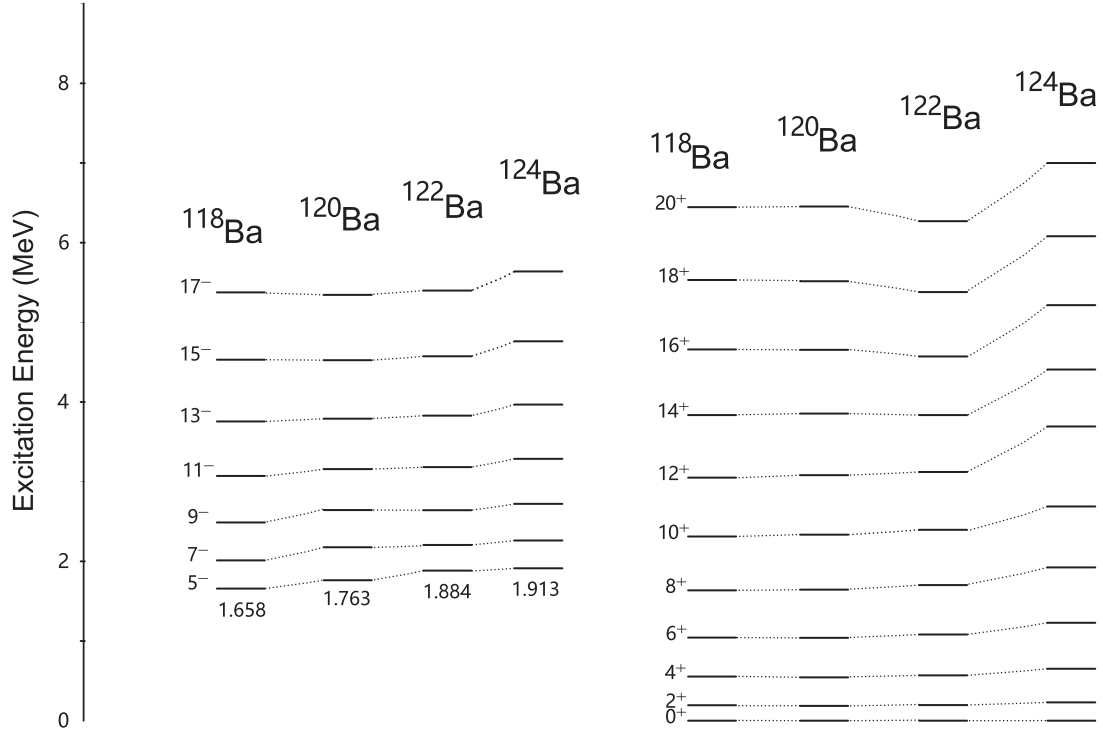


FIG. 5. Systematics of the negative-parity bands built on the  $5^-$  states and the ground-state bands in  $^{118,120,122,124}\text{Ba}$  nuclei.

to those of the other bands. The bands with similar slopes of  $E - 0.01107I(I + 1)$  have very similar moments of inertia (MOI), while the ground-state band below the upbending and the high-spin part of Band 2, have MOIs significantly lower and higher ( $\approx 25\%$ ), respectively (see Fig. 4).

Band 1 above the up-bend and Band 5 have similar excitation energies, as in the case of the bands built on the  $\pi h_{11/2}$  and  $\pi g_{9/2}$  orbitals in  $^{119}\text{Cs}$ , which are separated by only 25 keV (Bands 1 and 8 in Ref. [5]). Based on the similar excitation energies of the bands in  $^{119}\text{Cs}$  and  $^{120}\text{Ba}$ , the configurations of Band 1 above the up-bend and of Band 5 can be explained by coupling one proton in  $\pi h_{11/2}$  to the  $\pi h_{11/2}$  and  $\pi g_{9/2}^{-1}$  configurations in  $^{119}\text{Cs}$ , leading to the two-quasiparticle configurations  $\pi(h_{11/2})^2$  and  $\pi(h_{11/2}g_{9/2}^{-1})$ , respectively.

The low-spin part of Bands 2 and 3 also have similar excitation energies. The configuration assignment to the low-spin part of Band 2 in Ref. [2] is  $\nu(h_{11/2})^2$ , which is expected to be occupied at nearly identical rotational frequency as that of the  $\pi(h_{11/2})^2$  configuration assigned to Band 1 above the up-bend.

The configuration assigned to the negative-parity Bands 3 and 4 should involve low-lying opposite-parity orbitals in the odd-even neighboring  $^{119}\text{Ba}$  and  $^{119}\text{Cs}$ . Such orbitals have been recently assigned to the low-lying Bands 3 and 2 in  $^{119}\text{Ba}$ , which have band heads at 0 and 53 keV, and  $\nu g_{7/2}[411]3/2^+$  and  $\nu d_{5/2}[413]5/2^+$  configurations, respectively [4], as well as to Bands 4 and 5 in  $^{119}\text{Cs}$ , which have band-heads at 144 and 209 keV, and  $\pi d_{5/2}[420]1/2^+$  and  $\pi g_{7/2}[422]3/2^+$  configurations, respectively [5]. To pin down the nature of Bands 3 and 4, we plotted the systematics of the negative-parity bands built on the  $5^-$  states and the ground-

state bands, as well as the energy minus a rotating liquid drop  $E - E_{RLD}$  [11] of the corresponding bands observed in the neighboring  $^{118-124}\text{Ba}$  nuclei in Figs. 6 and 5, respectively, in which one can see the evolution as a function of the neutron number. As the bands in the  $^{118,122,124}\text{Ba}$  nuclei have been interpreted as two-proton configurations [1,3,27,30], we also assign a two-proton configuration to Bands 3 and 4 of  $^{120}\text{Ba}$ , with one proton in the  $\pi h_{11/2}[541]3/2^-$  orbital and the other proton in the  $\pi d_{5/2}[420]1/2^+$  orbital, which is strongly mixed with the close lying  $\pi g_{7/2}[422]3/2^+$  orbital. The present configuration assignment to Bands 3 and 4 is similar to that proposed in Ref. [8].

By assigning the  $(\pi h_{11/2})^2$  configuration to Band 1,  $\pi^2[541]3/2^-[420]1/2^+$  mixed with  $\pi^2[541]3/2^-[422]3/2^+$  to Bands 3 and 4, and  $\pi(h_{11/2}g_{9/2}^{-1})$  to Band 5, one obtains an interpretation coherent with the observed low-lying configurations  $\pi h_{11/2}$ ,  $\pi d_{5/2}[420]1/2^+$ ,  $\pi g_{7/2}[422]3/2^+$ , and  $\pi g_{9/2}^{-1}$  in  $^{119}\text{Cs}$ , respectively. One can therefore conclude that the coupling of an  $h_{11/2}$  proton with the low-lying proton configurations in  $^{119}\text{Cs}$  induces, as expected, configurations with nearly similar relative excitation energies in  $^{120}\text{Ba}$ . In Fig. 3(a) one can also see changes of the slopes along Bands 1 and 2, which can be due to either crossing between different configurations or shape changes in the same configuration. Hints on the possible shape changes will be discussed later, based on CNS and PNC-CSM calculations. In the following we discuss the alignment properties of the observed bands.

The quasiparticle aligned angular momenta  $i_x$  of the observed bands in  $^{120}\text{Ba}$  are shown in Fig. 3(b), and of selected



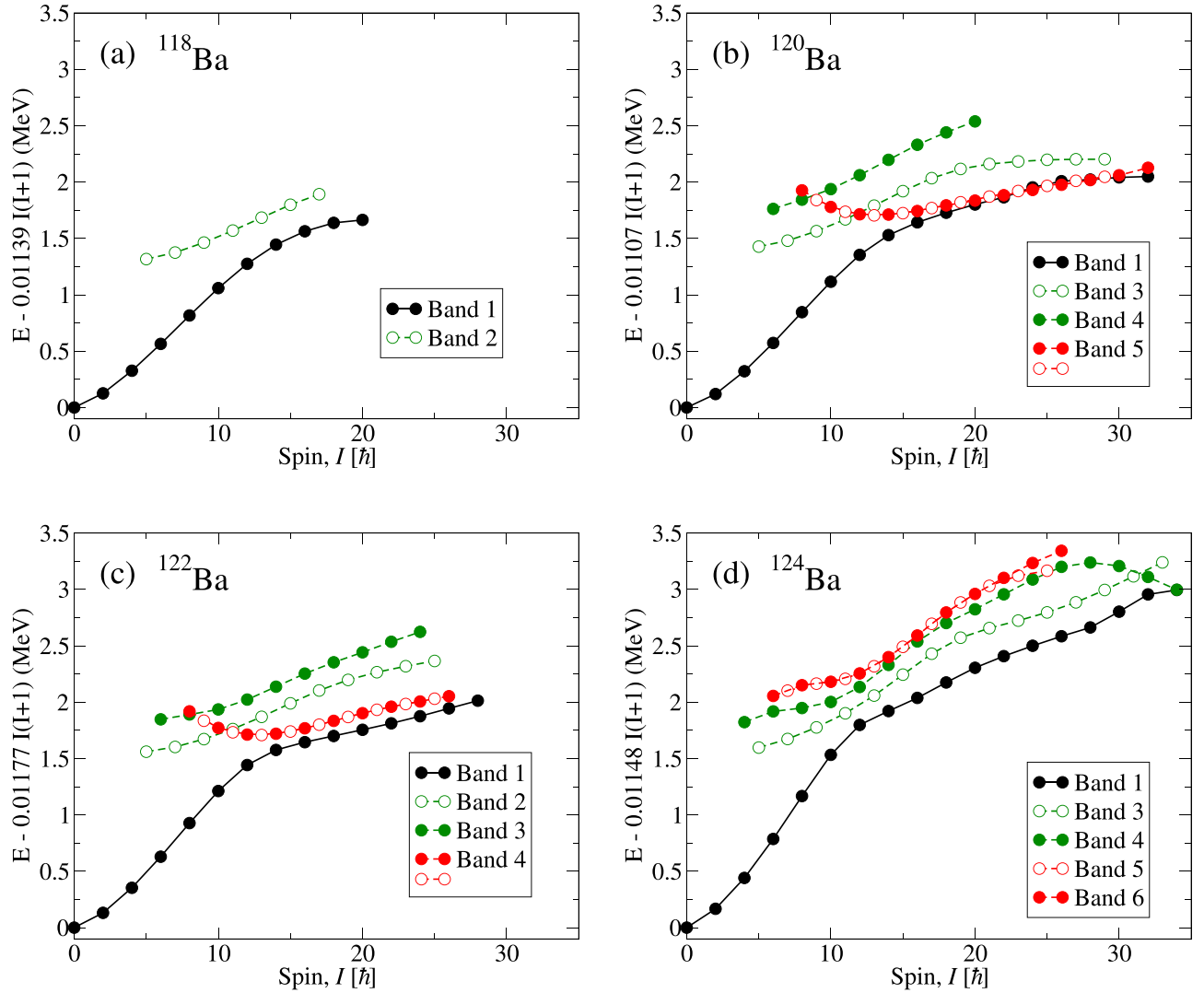


FIG. 6. Experimental excitation energy relative to a rotating liquid drop  $E - E_{RLD}$  [11] as a function of the spin for the bands of  $^{118}\text{Ba}$  [1],  $^{120}\text{Ba}$  (present work),  $^{122}\text{Ba}$  [30], and  $^{124}\text{Ba}$  [27] nuclei. The tentative spins of band 4 of  $^{122}\text{Ba}$  assigned in Ref. [30] have been increased by  $2\hbar$  to obtain the gradual change of the excitation energy of the strongly coupled bands (drawn in red) in the sequence of Ba nuclei.

bands in  $^{119}\text{Ba}$  and  $^{120}\text{Ba}$  in Fig. 7. In Fig. 3(b) one can see that the alignments of all bands saturate at values below  $11\hbar$ , except for Band 2, which reaches  $i_x$  values higher by  $\approx 3\hbar$  than those of the other bands, before turning down at the highest frequencies. This peculiar feature of Band 2 has been analyzed in Ref. [2], in which the  $i_x$  values have been compared with those of Band 2 in  $^{119}\text{Ba}$ , resulting to be similar after subtracting the alignment of the unpaired neutron present in the positive parity  $\nu(g_{7/2}/d_{5/2})$  ( $\nu d_{5/2}[413]5/2^-$  in Ref. [4]) configuration of  $^{119}\text{Ba}$ . The present results on  $^{120}\text{Ba}$  and those on  $^{119}\text{Ba}$  [4], confirm the results of Ref. [2], in which the four-quasiparticle configuration  $\pi(h_{11/2})^2 \otimes \nu(h_{11/2})^2$  has been assigned to the high-spin part of Band 2. However, as one can see in Fig. 1, the two out-of-band transitions from the  $22^+$  and  $24^+$  states of Band 2 are simply connecting transitions to states of Band 1, being induced by the crossing and associated

mixing between the bands. The claimed novel phenomenon of forking of the ground-state band in two bands and their recombination into a single band can in fact be simply explained by the crossing between the two-quasiparticle band built on the  $\pi(h_{11/2})^2$  configuration of Band 1 above the up-bend with the four-quasiparticle band built on the  $\pi(h_{11/2})^2 \otimes \nu(h_{11/2})^2$  configuration of Band 2 above the upbending, which occurs at  $I^\pi = 22^+$  or equivalently at a rotational frequency of  $\hbar\omega \approx 0.55$  MeV. As one can see in Fig. 3(b), the alignment in both Bands 1 and 2 are perturbed at frequencies around  $\approx 0.5$  MeV, due to the mixing of the states with  $I^\pi = 22^+$  and  $I^\pi = 24^+$ .

The alignment gain exhibited by Bands 3 and 4 at  $\approx 0.4$  MeV is smaller and more gradual than that in Band 1, which is induced by two  $h_{11/2}$  protons. This is in agreement with the assigned two-proton configuration involving only one proton in the  $h_{11/2}$  orbital, with the other proton occupying the

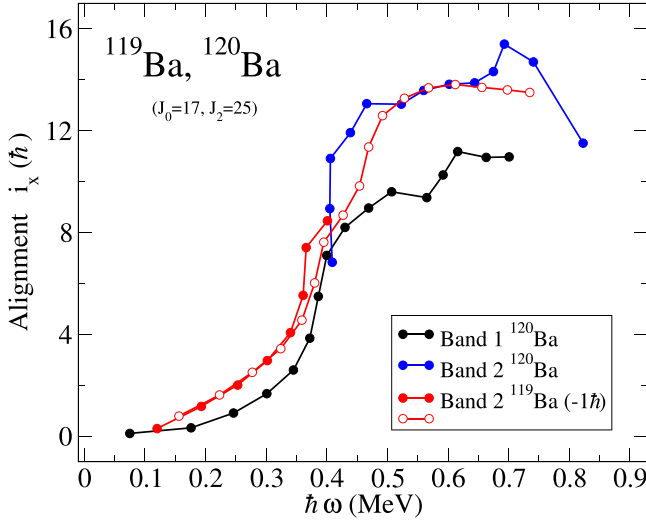


FIG. 7. Experimental single-particle aligned angular momenta  $i_x$  as function of the rotational frequency  $\hbar\omega$  for selected bands in  $^{119}\text{Ba}$  and  $^{120}\text{Ba}$ . The angular momentum of the core is parametrized with the Harris parameters  $\mathcal{J}_0 = 17 \hbar^2 \text{ MeV}^{-1}$  and  $\mathcal{J}_2 = 25 \hbar^4 \text{ MeV}^{-3}$ .

strongly mixed lower- $j$  Nilsson orbitals  $\pi d_{5/2}[420]1/2^+$  and  $\pi g_{7/2}[422]3/2^+$ .

The alignment of Band 5 composed of degenerate signature partners of  $\approx 5.5\hbar$  at the band head, can be accounted for by the occupation of the high- $\Omega$   $\pi[404]9/2^+$  extruder orbital, which carries a very small alignment, and the low- $\Omega$   $\pi[541]3/2^-$  orbital, which carries  $i_x \approx 5\hbar$ . The  $\pi^2[541]3/2^-[404]9/2^+$  configuration assignment to Band 5 is therefore supported by the experimental alignment.

### B. CNS and PNC-CSM calculations

To get further insight into the band structure of  $^{120}\text{Ba}$ , CNS, and PNC-CSM calculations have been performed. The CNS calculations of the possible configurations allowed to estimate the shape of a given configuration and its evolution with spin.

However, as in CNS calculations the pairing is neglected, the alignments and crossing frequencies are not well reproduced. The calculated quadrupole and triaxial deformations of the assigned configurations are listed in Table II, together with those reported in Ref. [2], which were obtained from total Routhian surface (TRS) calculations. One can see that both models predict similar quadrupole deformations, slightly higher by TRS calculations, while the calculated triaxial deformations for some configurations are quite different. However, the calculated quadrupole deformations are smaller by  $\approx 20\%$  than those used in the PNC-CSM calculations, which reproduce well the experimental data. Differences between calculated and experimental deformations have been discussed in our recent works on  $^{119}\text{Ba}$  [4] and  $^{119}\text{Cs}$  [5,24,25], which show that PNC-CSM calculations can well reproduce the band properties by adopting the experimental deformations measured for the bands heads. However, as the shape-driving properties of the orbitals do not change significantly with deformation, the relative magnitudes of the calculated quadrupole deformations can be used to understand the impact of different orbitals on the nuclear deformation, while the calculated triaxial deformation can be used to understand the evolution of the band properties as function of spin.

The PNC-CSM calculations have been performed assuming an axial deformation of  $\varepsilon_2 = 0.32$  for all bands, as in the case of the odd-even neighboring  $^{119}\text{Ba}$  and  $^{119}\text{Cs}$  nuclei [4,5,24,25], whose single-particle configurations are involved in the two-particle configurations of the bands in  $^{120}\text{Ba}$ .

As one can see in Fig. 8, the magnitude of the MOI and the frequency of the  $\pi(h_{11/2})^2$  alignment in Band 1 are well reproduced for  $\varepsilon_2 = 0.32$ . A successive gradual  $\nu(h_{11/2})^2$  alignment around  $\hbar\omega \approx 0.48$  is predicted, which leads to a good agreement of the projection of the angular momentum on the cranking axis  $J_x$  up to high frequencies, see Fig. 8(c). This good agreement between the PNC-CSM and experiment for Band 1 gives credence to the small triaxiality predicted by TRS calculations, and invalidates the large triaxiality calculated with CNS in which the pairing correlations are neglected.

TABLE II. Assigned configurations, experimental crossing frequencies  $\hbar\omega_{\text{exp}}$  in MeV, and deformation parameters ( $\beta_2$ ,  $\gamma$ ) calculated in Ref. [2] using the TRS model, and ( $\varepsilon_2$ ,  $\gamma$ ) calculated in the present work using the CNS model. The approximate relation between  $\beta_2$  and  $\varepsilon_2$  valid for small deformations is  $\varepsilon_2 \approx 0.95\beta_2$  [31].

Band	Configuration	$\hbar\omega_{\text{exp}}$	$\beta_2^{\text{TRS}}$	$\varepsilon_2^{\text{CNS}}$	$\gamma^{\text{TRS}}$	$\gamma^{\text{CNS}}$
Band 1 low	vacuum		0.28	0.25	$-5^\circ$	$-10^\circ$
Band 1 high	$\pi h_{11/2}^2$	0.38	0.26	0.26	$1^\circ$	$-20^\circ$
Band 2 low	$\nu h_{11/2}^2$	0.40	0.28	0.25	$-3^\circ$	$-2^\circ$
Band 2 medium	$\pi h_{11/2}^2 \otimes \nu h_{11/2}^2$		0.30	0.27	$-13^\circ$	$-15^\circ$
Band 2 high	$\pi h_{11/2}^2 \otimes \nu h_{11/2}^1 f_{7/2}^1$	0.68		0.20		$20^\circ$
Band 3 low	$\pi^2[541]3/2[420]1/2$			0.24		$17^\circ$
Band 3 high	$\pi^2[541]3/2[420]1/2 \otimes \nu h_{11/2}^2$			0.24		$-10^\circ$
Band 4 low	$\pi^2[541]3/2[422]3/2$			0.25		$17^\circ$
Band 4 high	$\pi^2[541]3/2[422]3/2 \otimes \nu h_{11/2}^2$	0.44		0.25		$17^\circ$
Band 5	$\pi^2[541]3/2[404]9/2$			0.27		$10^\circ$

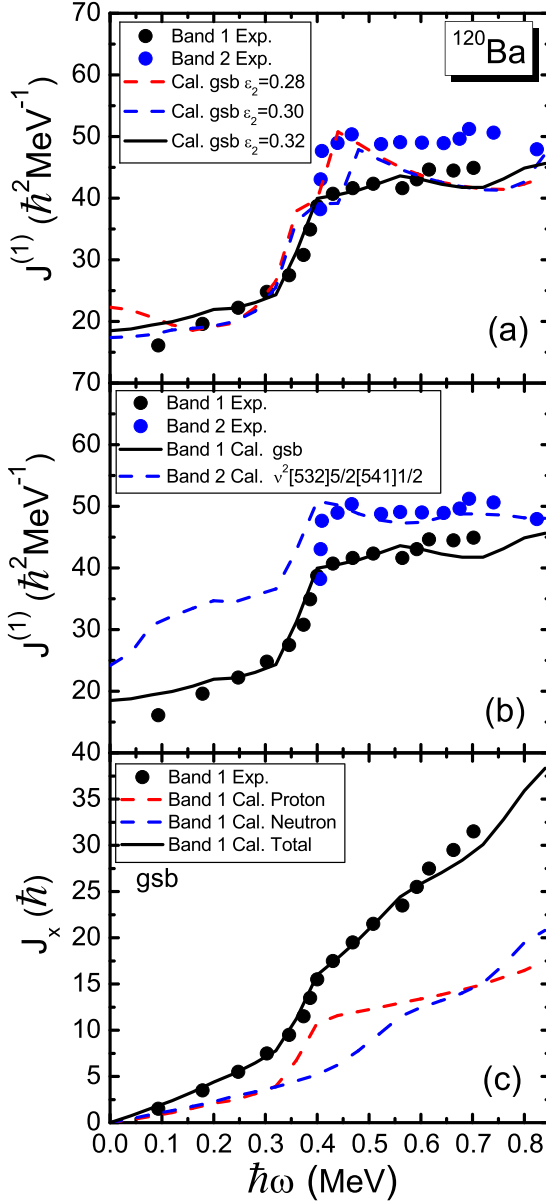


FIG. 8. (a) and (b) Moments of inertia  $J^{(1)}$ , and (c) projections of the angular momentum on the cranking axis  $J_x$  for Bands 1 and 2 of  $^{120}\text{Ba}$  calculated using the PNC-CSM model assuming axially symmetric shapes. The calculated values in (b) and (c) are for a deformation of  $\varepsilon_2 = 0.32$ .

As one can see in Fig. 8(a), the MOI of Band 2 is not reproduced for  $\varepsilon_2 = 0.32$ , thus a smaller deformation with  $\varepsilon_2 = 0.28$  was adopted. The MOI is therefore well reproduced around the crossing frequency because the alignment of protons and neutrons occurs at similar frequencies, but is underestimated at high frequency. This can be due to a change in deformation, as suggested by both TRS and CNS calculations, which predict a slight increase of the quadrupole deformation and a significant increase of the triaxial deformation from  $\gamma \approx -2^\circ$  around the crossing frequency to  $\gamma \approx -14^\circ$  at higher frequency. At  $\hbar\omega \approx 0.68$  MeV, an up-bend is observed in Band 2, which can be due to the crossing between

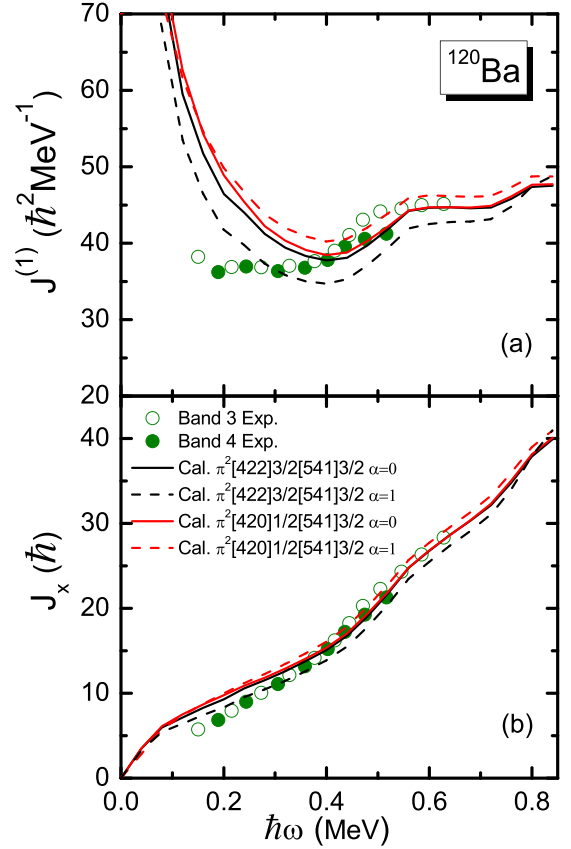


FIG. 9. (a) Moments of inertia  $J^{(1)}$ , (b) projections of the angular momentum on the cranking axis  $J_x$  for the  $\pi^2[422]3/2^+[541]3/2^-$ , and  $\pi^2[420]1/2^+[541]3/2^-$  configurations assigned to Bands 3 and 4 of  $^{120}\text{Ba}$  calculated using the PNC-CSM model assuming axially symmetric shapes.

the  $\nu h_{11/2}[532]5/2^-$  and  $\nu f_{7/2}[541]1/2^-$  orbitals. In fact, the  $\nu^2[532]5/2^-[541]1/2^-$  configuration, which is predicted to have a positive triaxiality of  $\gamma \approx 20^\circ$ , exhibits a MOI, which is in good agreement with the high-frequency part of the experimental band calculated for a deformation of  $\varepsilon_2 = 0.32$  [see Fig. 8(b)].

The MOIs of Bands 3 and 4 exhibit a gradual increase at  $\hbar\omega \approx 0.44$  MeV. The PNC-CSM calculations are in qualitative agreement with the experimental data in the crossing region if the mixed  $\pi^2[541]3/2^-[420]1/2^+ - \pi^2[541]3/2^-[422]3/2^+$  configuration is assigned. As one can see in Fig. 9, the MOIs and  $J_x$  are well reproduced around the crossing frequency and above, but the high calculated  $J^{(1)}$  at low frequency is not observed experimentally. This suggests a more complex configuration at low spin, which is beyond the present PNC-CSM calculations for axially symmetric shapes. The possible alternative negative-parity  $\nu^2[532]5/2[411]3/2$  and  $\nu^2[532]5/2[413]5/2$  configurations, which can describe Bands 3 and 4 were also investigated, see Fig. 10. However, the experimental alignment in the crossing region is not well reproduced and we can safely discard it.

As will be discussed in the following, the PNC-CSM calculations including octupole collectivity can achieve a better description of the negative-parity bands at low spin. The

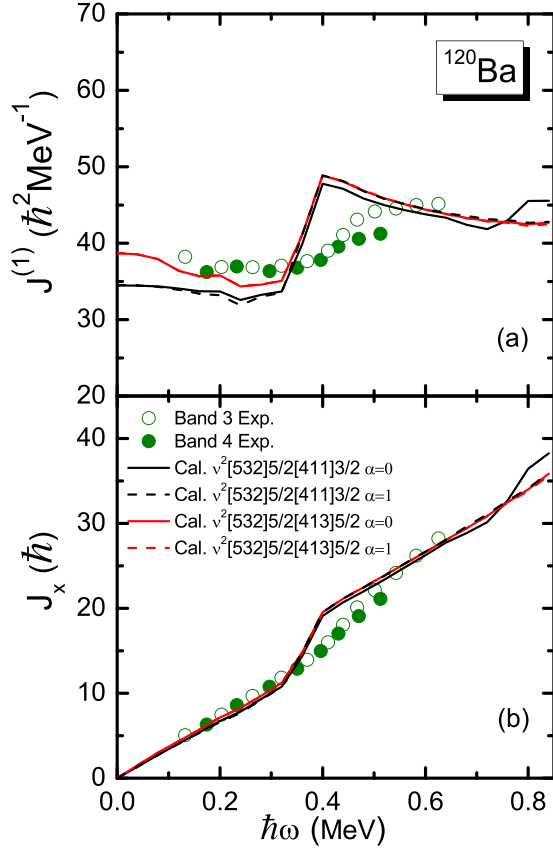


FIG. 10. (a) Moments of inertia  $J^{(1)}$ , (b) projections of the angular momentum on the cranking axis  $J_x$  for the  $\nu^2[532]5/2^-[411]3/2^+$ , and  $\nu^2[532]5/2^-[413]5/2^+$  configurations calculated using the PNC-CSM model assuming axially symmetric shapes.

calculations for the neighboring  $^{118,122,124}\text{Ba}$  nuclei shown in Fig. 11 exhibit a similar behavior at low frequency, where the MOIs of the odd-spin bands are overestimated. One should also note that the CNS calculations for Band 3 show an increase of the triaxiality from  $\gamma \approx 17^\circ$  below the crossing to  $\gamma \approx -10^\circ$  above the crossing, while not such a shape change is calculated for Band 4 (see Table II).

### C. Possible octupole correlations

In order to investigate the octupole collectivity in the negative-parity bands, we performed PNC-CSM calculations using the formalism based on an octupole-deformed Nilsson potential, which was successfully applied to the alternating-parity bands in  $^{236,238}\text{U}$  and  $^{238,240}\text{Pu}$  [15]. The results of the calculations for Band 1, 3, and 4 of  $^{120}\text{Ba}$  are shown in Fig. 12. One can see that the MOI of the ground-state Band 1 is well reproduced over the entire frequency range, like in the calculations for axially symmetric shapes (see Fig. 8), while those of Bands 3 and 4 are in very good agreement with the experimental values down to the lowest observed frequencies for an octupole deformation  $\varepsilon_3 = 0.003$ , a behavior opposite to that of the MOIs calculated without

octupole deformation for the two-quasiparticle configurations  $\pi^2[541]3/2^-[420]1/2^+$  and  $\pi^2[541]3/2^-[422]3/2^+$ , which are much higher than the experimental values at low frequency (see Fig. 9). As the experimental MOIs are better reproduced by assuming reflection-asymmetric shapes, one can conclude that the negative-parity Bands 3 and 4 are built on two-quasiparticle configurations with significant octupole collectivity. A similar conclusion can be drawn for the negative-parity bands in the neighboring  $^{118,122,124}\text{Ba}$ , which exhibit MOIs similar to those of  $^{120}\text{Ba}$  (see Fig. 11).

From the measured intensities of the out-of-band  $E1$  and in-band  $E2$  transitions of the negative-parity bands, we extracted the ratios of reduced transition probabilities  $B(E1)/B(E2)$  shown in Fig. 13 and Table III, together with the values of neighboring Ba and Xe isotopes. These ratios are expected to increase with increasing octupole correlations [1,3]. The measured values for Ba nuclei are smaller than those in the Xe nuclei, have values similar to those of the negative-parity bands in other neighboring nuclei (see, e.g., Ref. [32]), and exhibit a slight decrease with decreasing neutron number. This is surprising, because intuitively one would expect an increase of the octupole correlations when the neutron number decreases towards the  $N = 56$  magic number for octupole correlations.

In order to understand this surprising behavior of the experimental  $B(E1)/B(E2)$  ratios, we performed calculations using the quadrupole and octupole collective Hamiltonian based on the relativistic Hartree-Bogoliubov (QOCH-RHB) model [16], employing the DD-PC1 density functional [17]. The  $B(E1)$  values are calculated as follows: first, we perform a constrained relativistic Hartree-Bogoliubov (RHB) calculation to obtain the intrinsic dipole moments  $D_0$  in the  $(\beta_2, \beta_3)$  plane using the dipole moment operator  $D = e_A^N r_p - e_A^N r_n$  (Eq. (11) in Ref. [33]); second, the QOCH with parameters determined by the constrained RHB calculation is solved to obtain the collective wave functions for the ground and excited states; finally, we calculate the  $B(E1)$  values by integrating the dipole moment  $D_0$  and the collective wave functions of the initial and final states in the  $(\beta_2, \beta_3)$  plane. Figure 15 displays the calculated intrinsic dipole moments  $D_0$  in the  $(\beta_2, \beta_3)$  plane for the Ba and Xe isotopes. Meanwhile, the expectation deformations for the states  $7^-$  and  $9^-$  are also shown by the blue and red diamonds, which are calculated from the corresponding collective wave functions (see Fig. 16). It is interesting to find that the deformation dependence of the microscopic intrinsic dipole moments  $D_0$  is quite different from that of the liquid-drop model  $D_0 = C_{LD} A Z e \beta_2 \beta_3$  (Eq. (92) in Ref. [33]). This could be because the dipole moments are rather sensitive to the single-particle properties and cancellation effects. According to the procedure used in the present QOCH-RHB calculations, the  $B(E1)$  values are generally dominated by the dipole moments  $D_0$  around the peak of the collective state (see Fig. 16 and diamonds in Fig. 15). Therefore, from  $^{122}\text{Ba}$  to  $^{116}\text{Ba}$ , the absolute values of the corresponding  $D_0$  dipole moments decrease gradually while the  $E2$  transitions are almost unchanged (see Fig. 17), thus leading to the down slope of the  $B(E1)/B(E2)$

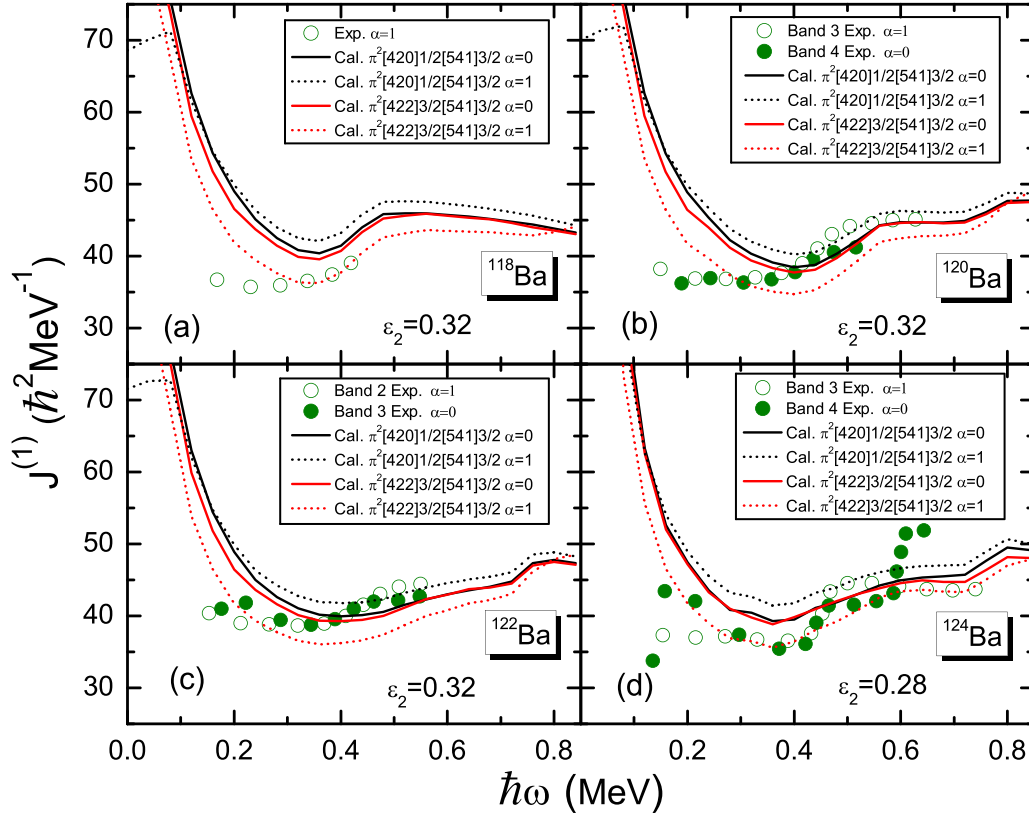


FIG. 11. Experimental moments of inertia  $J^{(1)}$  of the negative-parity bands in  $^{118}\text{Ba}$  [1],  $^{120}\text{Ba}$  (present work),  $^{122}\text{Ba}$  [30], and  $^{124}\text{Ba}$  [27] compared with those calculated using the PNC-CSM model assuming axially symmetric shapes with deformation  $\varepsilon_2 = 0.32$  for  $^{118,120,122}\text{Ba}$  and  $\varepsilon_2 = 0.28$  for  $^{124}\text{Ba}$ .

values with decreasing neutron number. However, from  $^{114}\text{Ba}$  to  $^{112}\text{Ba}$ , the  $|D_0|$  dipole moments increase, explaining thus the increase of the  $B(E1)/B(E2)$  ratios. For the whole Xe isotopes, the  $|D_0|$  values around the peaks of the collective states

decrease gradually over the entire sequence from heavy to light nuclei.

Calculated potential energy surfaces and energy spectra for  $^{112-124}\text{Ba}$  and  $^{110-120}\text{Xe}$  are given in Figs. 17–19. In Table IV

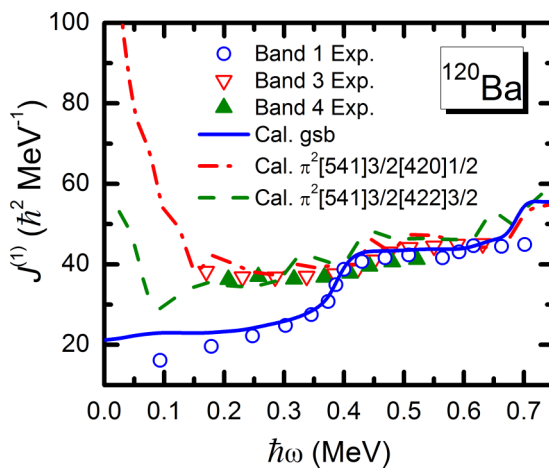


FIG. 12. Moment of inertia  $J^{(1)}$  for bands 1, 3, and 4 of  $^{120}\text{Ba}$  calculated using the PNC-CSM model assuming reflection-asymmetric shapes with deformation parameters  $\varepsilon_2 = 0.32$ ,  $\varepsilon_2 = 0.003$ .

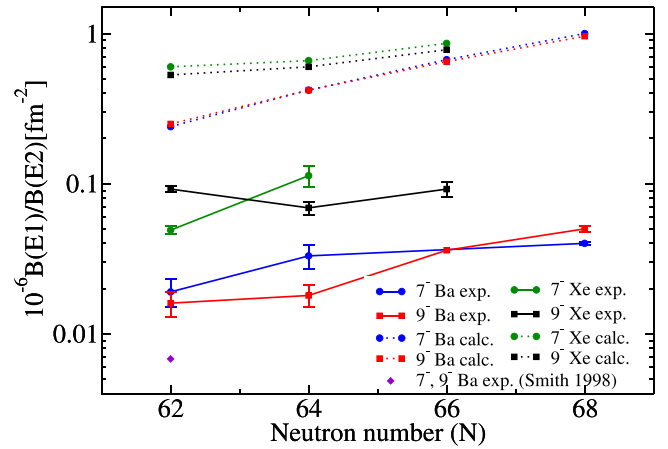


FIG. 13. Comparison between experimental ratios of reduced transition probabilities  $B(E1)/B(E2)$  and those calculated using the QOCH-RHB model for light Ba and Xe nuclei. The experimental values are from Ref. [1] for  $^{118}\text{Ba}$ , from the present work for  $^{120}\text{Ba}$ , from Ref. [26] for  $^{122}\text{Ba}$ , from Ref. [3] for  $^{124}\text{Ba}$ , from Ref. [28] for  $^{116}\text{Xe}$ , from Ref. [29] for  $^{118}\text{Xe}$ , from Ref. [29] for  $^{120}\text{Xe}$ .



TABLE III. Experimental and calculated with the QOCH-RHB model  $B(E1)/B(E2)$  ratios for the  $7^-$  and  $9^-$  transitions in  $^{118-124}\text{Ba}$  and  $^{116-120}\text{Xe}$  nuclei, respectively.

	$10^{-6}B(E1)/B(E2)$ (fm $^{-2}$ ) $7^- \rightarrow 6^+$ (Expt.)	QOCH-RHB $7^- \rightarrow 6^+$	$10^{-6}B(E1)/B(E2)$ (fm $^{-2}$ ) $9^- \rightarrow 8^+$ (Expt.)	QOCH-RHB $9^- \rightarrow 8^+$	References
$^{112}\text{Ba}$		1.01		1.10	Present work
$^{114}\text{Ba}$		1.43		0.15	Present work
$^{116}\text{Ba}$		0.79		0.08	Present work
$^{118}\text{Ba}$	0.007 <sup>a</sup>	0.24	0.007 <sup>a</sup>	0.25	[1]
$^{118}\text{Ba}$	0.019(4)	0.24	0.019(3)	0.25	Present work
$^{120}\text{Ba}$	0.033(6)	0.42	0.018(3)	0.42	Present work
$^{122}\text{Ba}$		0.67	0.036	0.65	[26]
$^{124}\text{Ba}$	0.040(11)	1.00	0.054(13)	0.96	[3]
$^{116}\text{Xe}$	0.049(3)	0.60	0.092(4)	0.53	[28]
$^{118}\text{Xe}$	0.113(18)	0.66	0.069(7)	0.60	[29]
$^{120}\text{Xe}$		0.86	0.092(11)	0.78	[29]

<sup>a</sup>Quadrupole moment of  $Q = 496 \text{ efm}^2$  was adopted from Ref. [1].

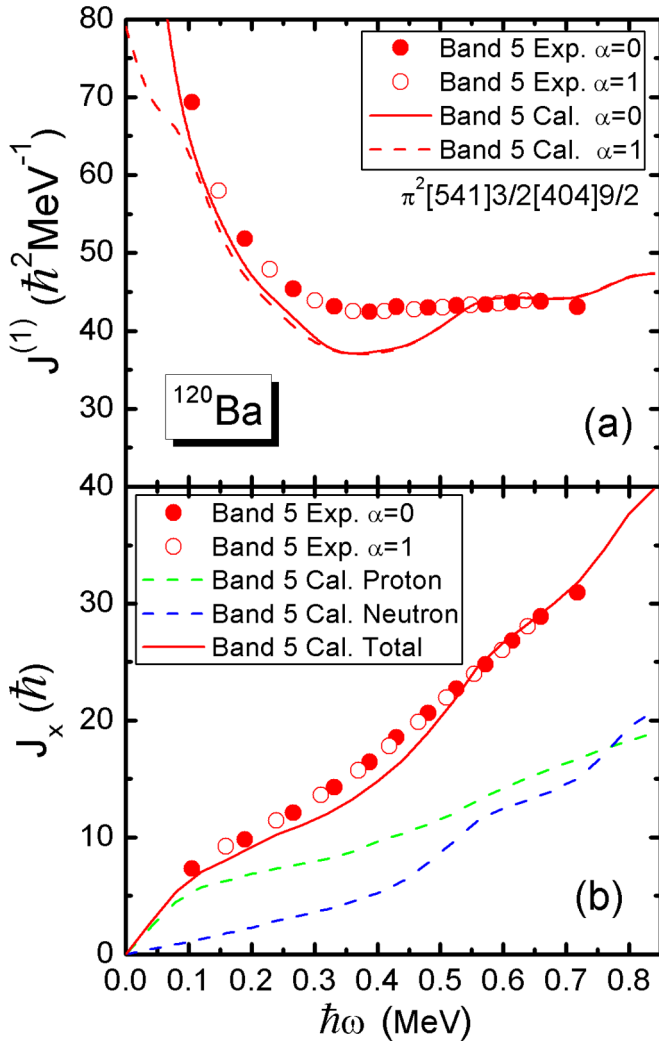


FIG. 14. (a) Moment of inertia  $J^{(1)}$ , (b) projection of the angular momentum on the cranking axis  $J_x$  for Band 5 of  $^{120}\text{Ba}$  calculated using the PNC-CSM model assuming axially symmetric shape with deformation  $\varepsilon_2 = 0.32$ . The states with signature  $\alpha = 0$  and  $\alpha = 1$  are drawn with filled and open symbols, respectively.

we list the deformation parameters ( $\beta_2, \beta_3$ ) for the global minima of the PESs in Fig. 17, which are calculated by the constrained relativistic Hartree-Bogoliubov without cranking.

One can observe the evolution of the octupole deformation with decreasing neutron number: softness along both  $\beta_2$  and  $\beta_3$  axes is present in the heavy isotopes, which evolves into well-established minima in  $^{112}\text{Ba}$  and  $^{114}\text{Ba}$ , narrow in  $\beta_2$  and wide in  $\beta_3$  directions. A similar evolution is also present in the Xe nuclei, with a minimum centered on the  $\beta_2$  axis which exhibits an increasing softness along the  $\beta_3$  axis and becomes narrower in the  $\beta_2$  direction for light nuclei. The calculated  $B(E3)$  values increase by a factor of two from  $^{124}\text{Ba}$  to  $^{114}\text{Ba}$  (see in Fig. 18), which indicate increasing octupole correlations with decreasing  $N$ , with  $^{114}\text{Ba}$  having the highest values. A similar evolution is present in the Xe nuclei, with the highest  $B(E3)$  values calculated for  $^{110}\text{Xe}$ . The calculated  $B(E1)$  values are rather high but have an opposite behavior, going down by a factor of 10 when going from  $^{124}\text{Ba}$  to  $^{114}\text{Ba}$ , and then jumping up in  $^{112}\text{Ba}$ .

The calculated  $K^\pi = 0^-$  bands lie 1–2 MeV higher than the experimental ones. The calculated  $B(E1)/B(E2)$  values reproduce the observed decreasing trend towards smaller neutron numbers, but are about one order of magnitude higher than the experimental ones. The calculated octupole softness in the  $\beta_2$ - $\beta_3$  plane and the high  $B(E1)/B(E2)$  values can be induced by the used density functional, but can also correspond to higher-lying negative-parity bands, which are yet unobserved experimentally. The  $^{112-122}\text{Ba}$  and  $^{110-120}\text{Xe}$  spectra can also be checked for octupole collectivity by the collective quadrupole-octupole rotation model (QORM) [34], as recently done for  $^{136}\text{Nd}$  [32], in which enhanced octupole correlations were observed at high spin. The energy spectra are well reproduced [35], which suggests the possible existence of octupole collectivity.

#### D. Strongly coupled Band 5

The negative-parity Band 5 has a configuration involving the strongly coupled  $\pi g_{9/2}[404]9/2^+$  and the decoupled  $\pi h_{11/2}[541]3/2^-$  orbitals present at low excitation energy in



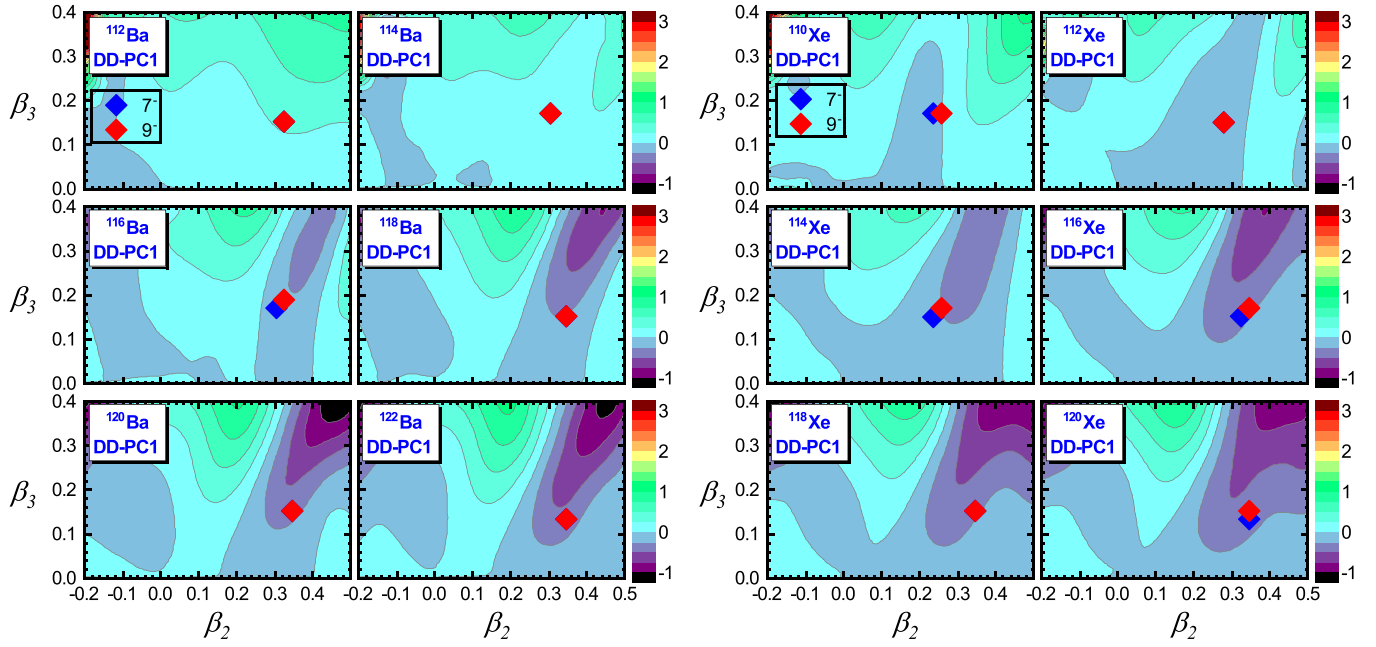


FIG. 15. The calculated intrinsic dipole moments  $D_0$  in the  $(\beta_2, \beta_3)$  plane for the Ba and Xe isotopes. The expectation deformations for the states  $7^-$  and  $9^-$  are also shown by the blue and red diamonds.

$^{119}\text{Cs}$  [5,24,25]. Similar bands have been observed in  $^{122,124}\text{Ba}$  [3,26,27] and in  $^{116,118,120}\text{Xe}$  [28,29]. Band 5 exhibits a MOI, which increases at low frequency as in the band built on the  $\pi h_{11/2}[541]3/2^-$  orbital in  $^{119}\text{Cs}$  [5,25]. The degeneracy of the cascades with even and odd spins indicates the

occupation of a high- $\Omega$  orbital, which must be the strongly coupled  $\pi g_{9/2}[404]9/2^+$  orbital. As one can see in Fig. 14 the MOI and  $J_x$  are well reproduced, therefore we assign the  $\pi^2[541]3/2^- [404]9/2^+$  configuration to Band 5.

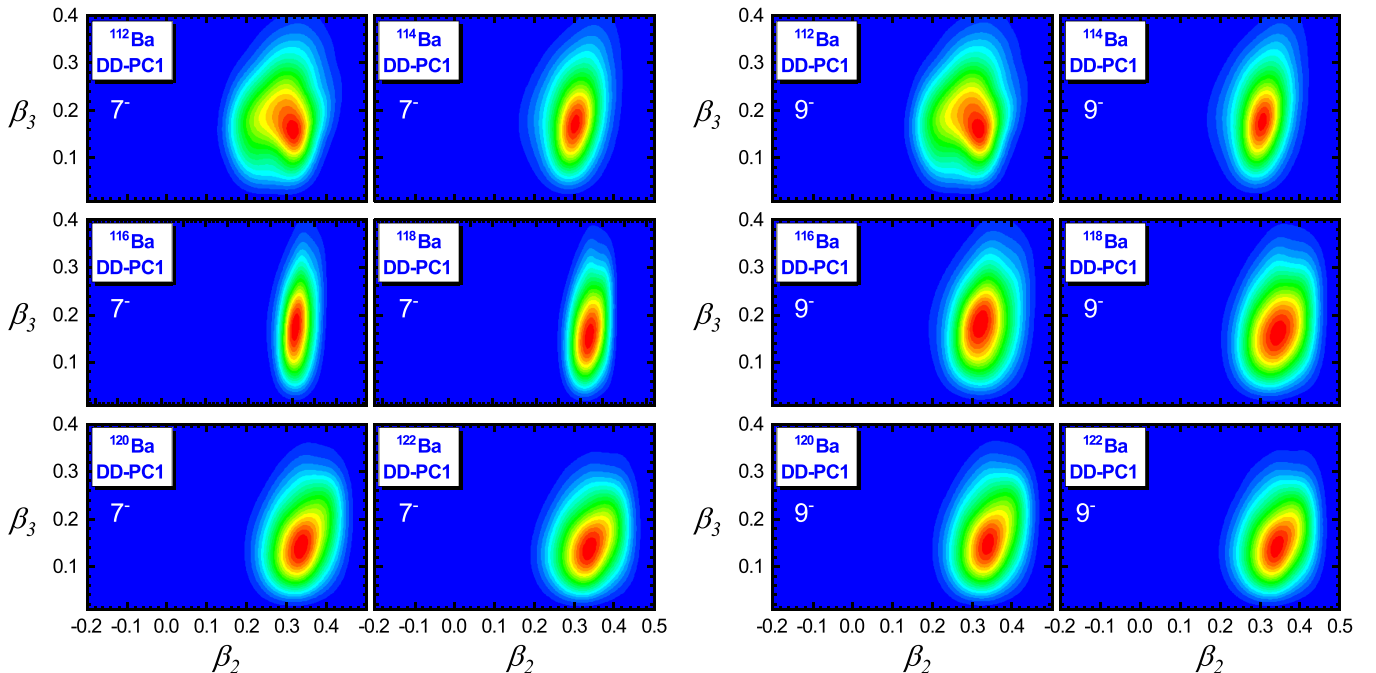


FIG. 16. The probability density distributions in the  $(\beta_2, \beta_3)$  plane for the  $7^-$  and  $9^-$  states in Ba isotopes, calculated with the QOCH model.

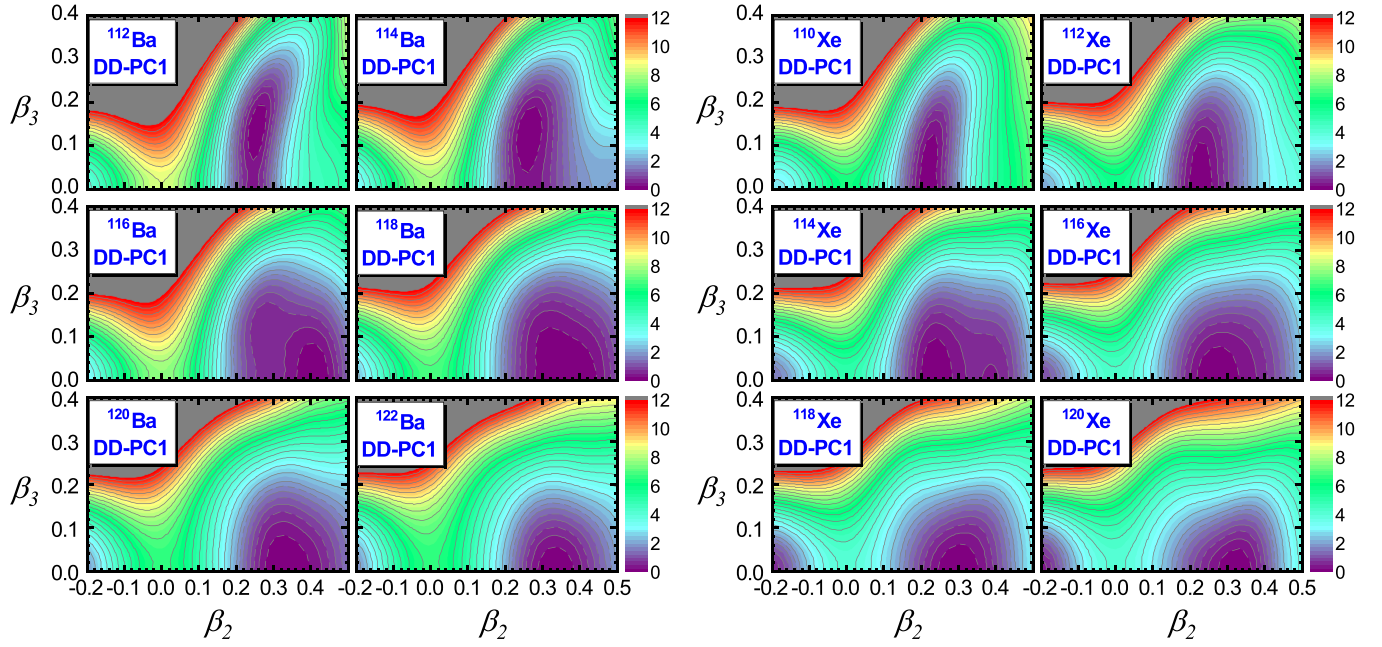


FIG. 17. Potential energy surfaces of  $^{112-122}\text{Ba}$  and  $^{110-120}\text{Xe}$  in the  $(\beta_2, \beta_3)$  deformation plane, calculated with the RHB model using the DD-PC1 density functional. The calculated PESs of  $^{114-122}\text{Ba}$  have been presented in Ref. [36].

#### IV. SUMMARY

In summary, the present work reports three new negative-parity bands in  $^{120}\text{Ba}$ , and examines the band structure using the CNS, PNC-CSM, and QOCH-RHB models. A good agreement between the theoretical calculations and experimental data is achieved for all bands. The crossing frequencies are reproduced by adopting a deformation 20% larger than that predicted by TRS and CNS calculations. The alignment of Band 2 at high spin is suggested to be due to the occupation of the  $\nu f_{7/2}$  intruder orbital, which crosses the  $\nu h_{11/2}$  orbital at high frequency. A simple explanation of the positive-parity bands at high spin is proposed. The comparison of the observed band structure with those of the odd-even  $^{119}\text{Ba}$  and

$^{119}\text{Cs}$  neighboring nuclei leads to consistent configuration assignments based on PNC-CSM calculations. The extent of octupole correlations in the negative-parity bands is also investigated in the light Ba and Xe nuclei. The calculated  $B(E1)/B(E2)$  values using the QOCH-RHB model reproduce the decreasing trend towards lower neutron numbers and the higher values in Xe nuclei, but are an order of magnitude higher than the experimental values. The PNC-CSM calculations including octupole deformation of the two-proton configuration  $\pi h_{11/2} \otimes \pi(d_{5/2}, g_{7/2})$  assigned to the bands built on the  $5^-$  and  $6^-$  states, reproduce very well the experimental data, suggesting the possible existence of moderate octupole collectivity in the negative-parity bands of nuclei in this mass region.

#### ACKNOWLEDGMENTS

This work has been supported by the Special Research Assistant Project of the Chinese Academy of Sciences; by the CAS “Light of West China” (Grant No. E123261YXB); by the China Scholarship Council (CSC), CSC No. 201804910386; by the National Natural Science Foundation of China (Grants No. U2032138 and No. 11775112); by the EU 7th Framework Programme Project No. 262010 (ENSAR); by the United Kingdom Science and Technology Facilities Council; by the National Research, Development and Innovation Fund of Hungary (Project No. K128947), as well as by the European Regional Development Fund (Contract No. GINOP-2.3.3-15-2016-00034); by the Swedish Research Council under Grant No. 2019-04880. C.A. is supported by the Natural Sciences and Engineering Research Council of Canada. The use of germanium detectors from the GAMMAPOOL is acknowledged. I.K. was supported by National Research, Development and Innovation Office-NKFIH, Contract No. PD 124717.

TABLE IV. The deformation parameters  $(\beta_2, \beta_3)$ , and the quadrupole moments for neutrons ( $Q_n$ ), for protons ( $Q_p$ ), and total ( $Q_{\text{total}}$ ) calculated at the minima of the PES figures of Fig. 14.

	$(\beta_2, \beta_3)$	$Q_n(\text{efm}^2)$	$Q_p(\text{efm}^2)$	$Q_{\text{total}}(\text{efm}^2)$
$^{112}\text{Ba}$	(0.27, 0.21)	373.85	395.68	769.53
$^{114}\text{Ba}$	(0.26, 0.14)	376.44	377.30	753.74
$^{116}\text{Ba}$	(0.41, 0)	628.86	597.56	1226.43
$^{118}\text{Ba}$	(0.38, 0)	617.06	560.15	1177.22
$^{120}\text{Ba}$	(0.33, 0)	560.29	474.85	1035.14
$^{122}\text{Ba}$	(0.33, 0)	590.97	485.26	1076.23
$^{124}\text{Ba}$	(0.32, 0)	604.16	480.27	1084.44
$^{110}\text{Xe}$	(0.22, 0.04)	311.60	300.55	612.15
$^{112}\text{Xe}$	(0.22, 0)	330.48	302.01	632.49
$^{114}\text{Xe}$	(0.23, 0)	368.26	316.99	685.25
$^{116}\text{Xe}$	(0.26, 0)	431.63	350.21	781.85
$^{118}\text{Xe}$	(0.30, 0)	511.56	404.36	915.92
$^{120}\text{Xe}$	(0.32, 0)	574.60	448.76	1023.36

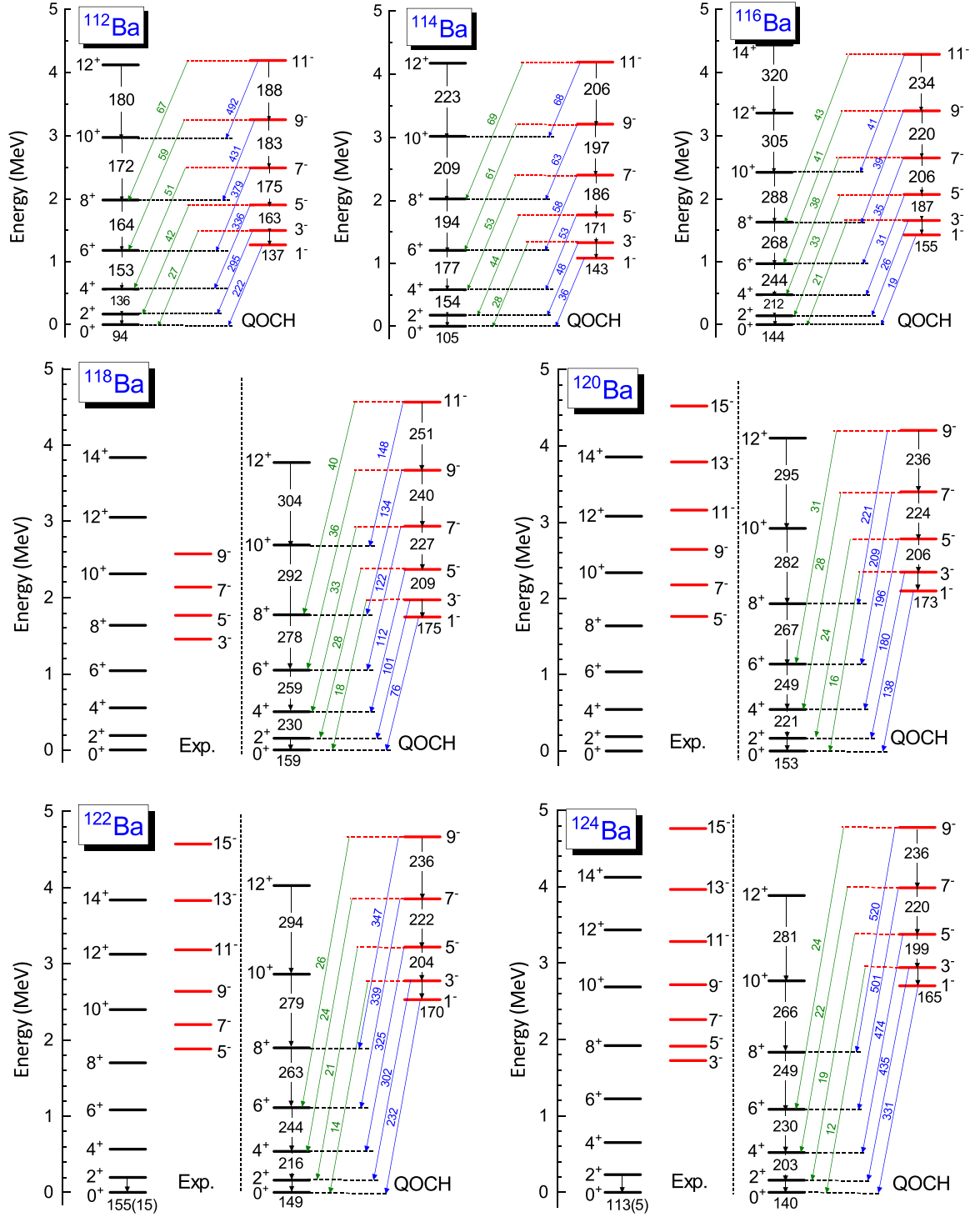


FIG. 18. The excitation spectrum, intraband  $B(E2)$  (W. u.) (in black), interband  $B(E1)$  ( $\times 10^{-5}$  W. u.) (in blue) and  $B(E3)$  (W. u.) (in green) values of  $^{112-124}\text{Ba}$  calculated with the QOCH based on DD-PC1 relativistic density functional, compared to experimental results.

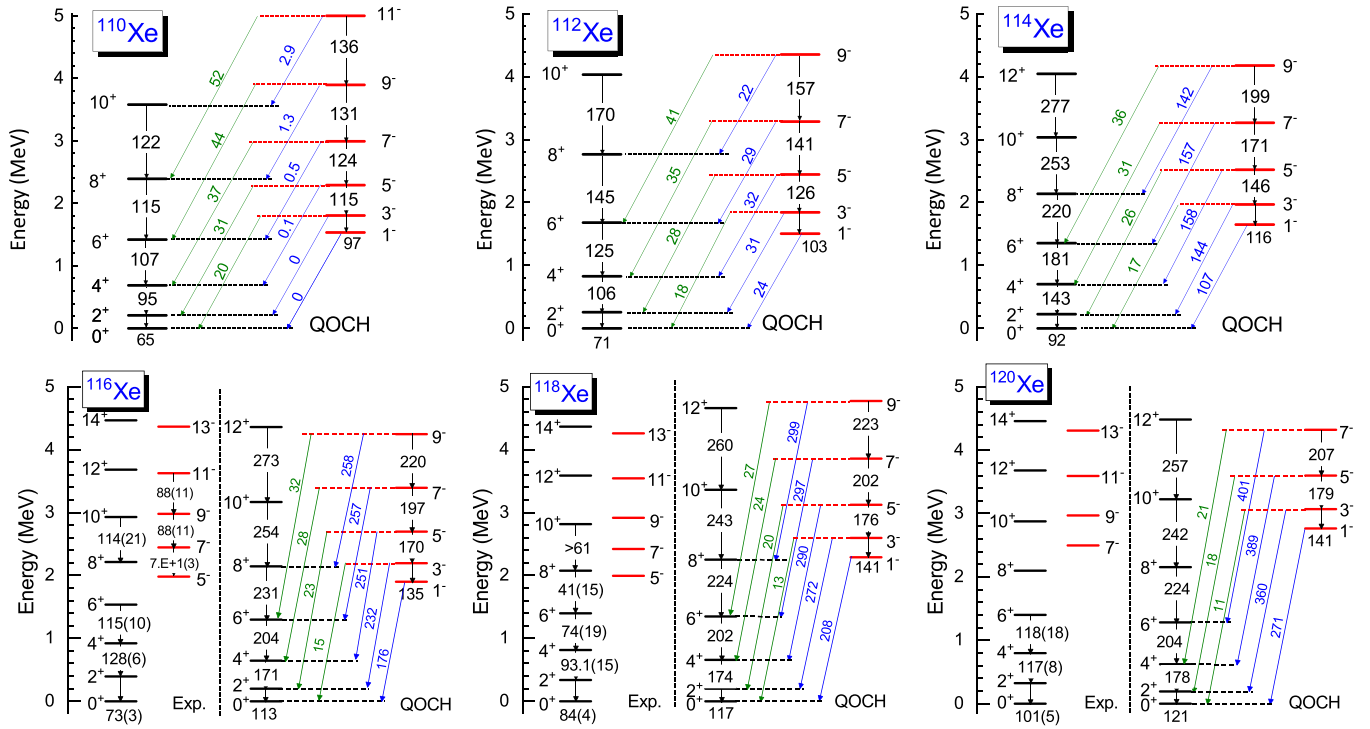


FIG. 19. The excitation spectrum, intraband  $B(E2)$  (W. u.) (in black), interband  $B(E1)$  ( $\times 10^{-5}$  W. u.) (in blue) and  $B(E3)$  (W. u.) (in green) values of  $^{110-120}\text{Xe}$  calculated with the QOCH based on DD-PC1 relativistic density functional, compared to experimental results.

- [1] J. F. Smith *et al.*, *Phys. Rev. C* **57**, R1037(R) (1998).
- [2] J. F. Smith, C. J. Chiara, D. B. Fossan, G. J. Lane, J. Sears, I. Thorslund, I. M. Hibbert, R. Wadsworth, I. Y. Lee, and A. O. Macchiavelli, *Phys. Lett. B* **483**, 7 (2000).
- [3] P. Mason *et al.*, *Phys. Rev. C* **72**, 064315 (2005).
- [4] K. K. Zheng, C. M. Petrache, Z. H. Zhang, A. Astier, B. F. Lv, P. T. Greenlees, T. Grahm, R. Julin, S. Juutinen, M. Luoma, J. Ojala, J. Pakarinen, J. Partanen, P. Rahkila, P. Ruotsalainen, M. Sandzelius, J. Saren, H. Tann, J. Uusitalo, G. Zimba, B. Cederwall, O. Aktas, A. Ertoprak, W. Zhang, S. Guo, M. L. Liu, X. H. Zhou, I. Kuti, B. M. Nyako, D. Sohler, J. Timar, C. Andreoiu, M. Doncel, D. T. Joss, and R. D. Page, *Phys. Rev. C* **104**, 014326 (2021).
- [5] K. K. Zheng, C. M. Petrache, Z. H. Zhang, A. Astier, B. F. Lv, P. T. Greenlees, T. Grahm, R. Julin, S. Juutinen, M. Luoma, J. Ojala, J. Pakarinen, J. Partanen, P. Rahkila, P. Ruotsalainen, M. Sandzelius, J. Saren, H. Tann, J. Uusitalo, G. Zimba, B. Cederwall, O. Aktas, A. Ertoprak, W. Zhang, S. Guo, M. L. Liu, X. H. Zhou, I. Kuti, B. M. Nyako, D. Sohler, J. Timar, C. Andreoiu, M. Doncel, D. T. Joss, and R. D. Page, *Phys. Rev. C* **104**, 044305 (2021).
- [6] C. Thibault *et al.*, *Nucl. Phys. A* **367**, 1 (1981).
- [7] N. J. Stone, *At. Data Nucl. Data Tables* **90**, 75 (2005).
- [8] B. Cederwall, A. Johnson, R. Wyss, F. Lidén, B. Fant, S. Juutinen, P. Ahonen, S. Mitarai, J. Mukai, and J. Nyberg, *Z. Phys. A* **338**, 461 (1991).
- [9] A. Afanasjev, D. Fossan, G. Lane, and I. Ragnarsson, *Phys. Rep.* **322**, 1 (1999).
- [10] T. Bengtsson and I. Ragnarsson, *Nucl. Phys. A* **436**, 14 (1985).
- [11] B. G. Carlsson and I. Ragnarsson, *Phys. Rev. C* **74**, 011302(R) (2006).
- [12] A. Afanasjev and I. Ragnarsson, *Nucl. Phys. A* **591**, 387 (1995).
- [13] J. Y. Zeng, T. H. Jin, and Z. J. Zhao, *Phys. Rev. C* **50**, 1388 (1994).
- [14] Z. H. Zhang, M. Huang, and A. V. Afanasjev, *Phys. Rev. C* **101**, 054303 (2020).
- [15] X.-T. He and Y.-C. Li, *Phys. Rev. C* **102**, 064328 (2020).
- [16] W. Sun, S. Quan, Z. P. Li, J. Zhao, T. Niksic, and D. Vretenar, *Phys. Rev. C* **100**, 044319 (2019).
- [17] T. Nikšić, D. Vretenar, and P. Ring, *Phys. Rev. C* **78**, 034318 (2008).
- [18] J. Pakarinen *et al.*, *Eur. Phys. J. A* **56**, 149 (2020).
- [19] J. Sarén *et al.*, *Nucl. Instrum. Meth. Phys. Res. B* **266**, 4196 (2008).
- [20] I. H. Lazarus *et al.*, *IEEE Trans. Nucl. Sci.* **48**, 567 (2001).
- [21] P. Rahkila, *Nucl. Instrum. Meth. Phys. Res. A* **595**, 637 (2008).
- [22] D. Radford, *Nucl. Instrum. Meth. Phys. Res. A* **361**, 297 (1995).
- [23] D. Radford, *Nucl. Instrum. Meth. Phys. Res. A* **361**, 306 (1995).
- [24] K. K. Zheng *et al.*, *Eur. Phys. J. A* **58**, 50 (2022).
- [25] K. K. Zheng *et al.*, *Phys. Lett. B* **822**, 136645 (2021).
- [26] C. Fransen, N. Pietralla, A. Linnemann, V. Werner, and R. Bijker, *Phys. Rev. C* **69**, 014313 (2004).
- [27] A. Al-Khatib *et al.*, *Phys. Rev. C* **74**, 014305 (2006).
- [28] J. M. Sears, D. B. Fossan, G. R. Gluckman, J. F. Smith, I. Thorslund, E. S. Paul, I. M. Hibbert, and R. Wadsworth, *Phys. Rev. C* **57**, 2991 (1998).

- [29] S. Törmänen *et al.*, [Nucl. Phys. A](#) **572**, 417 (1994).
- [30] C. M. Petrache *et al.*, [Eur. Phys. J. A](#) **12**, 135 (2001).
- [31] P. Möller, A. J. Slerk, T. Ichikawa, and H. Sagawa, [At. Data Nucl. Data Tables](#) **109-110**, 1 (2016).
- [32] C. M. Petrache, N. Minkov, T. Nakatsukasa, B. F. Lv, A. Astier, E. Dupont, K. K. Zheng, P. Greenlees, H. Badran, T. Calverley, D. M. Cox, T. Grahn, J. Hilton, R. Julin, S. Juutinen, J. Konki, J. Pakarinen, P. Papadakis, J. Partanen, P. Rahkila, P. Ruotsalainen, M. Sandzelius, J. Saren, C. Scholey, J. Sorri, S. Stolze, J. Uusitalo, B. Cederwall, A. Ertoprak, H. Liu, S. Guo, M. L. Liu, J. G. Wang, X. H. Zhou, I. Kuti, J. Timar, A. Tucholski, J. Srebrny, and C. Andreoiu, [Phys. Rev. C](#) **102**, 014311 (2020).
- [33] P. A. Butler and W. Nazarewicz, [Rev. Mod. Phys.](#) **68**, 349 (1996).
- [34] N. Minkov, P. Yotov, S. Drenska, and W. Scheid, [J. Phys. G: Nucl. Part. Phys.](#) **32**, 497 (2006).
- [35] N. Minkov (private communication).
- [36] S. Wei, S. Quan, J. Xiang, and Z. Li, [Nucl. Phys. Rev.](#) **36**, 144 (2019).